Received XX Month, XXXX; revised XX Month, XXXX; accepted XX Month, XXXX; Date of publication XX Month, XXXX; date of current version XX Month, XXXX.

Digital Object Identifier 10.1109/XXXX

Sensing-Based Spectrum Access in UAV-Enabled Cellular Networks

MD ASIF SYED[1] *(Senior Member, IEEE)*, HONGXIANG LI[1] *(Senior Member, IEEE)*, MARTIN HAENGGI[2] *(Fellow, IEEE)*, and ERIC J. KNOBLOCK[3]

[1]Department of Electrical and Computer Engineering, University of Louisville, Louisville, KY 40292 USA
[2]Department of Electrical Engineering, University of Notre Dame, Notre Dame, IN 46556 USA
[3]Glenn Research Center, NASA, Cleveland, OH 44135 USA

CORRESPONDING AUTHOR: HONGXIANG LI (e-mail: h.li@louisville.edu)

ABSTRACT This paper presents a novel spectrum sensing and sharing framework for unmanned aerial vehicle (UAV)-enabled cellular networks to efficiently reuse licensed spectrum. We investigate spectrum holes in a large-scale ground base station (GBS) network sensed by UAVs and analyze the network performance when UAVs opportunistically reuse the licensed spectrum. The received power at the UAVs originating from a GBS network is characterized, and an energy detection scheme is employed to identify the spectrum holes. To evaluate the performance of the spectrum sensing, we derive the exact error probabilities in the detection scheme. Using a log-normal approximation, the Neyman-Pearson framework is applied to derive a closed-form expression that minimizes the probability of missed detection under a fixed false alarm constraint. Furthermore, the complexity and performance of the proposed scheme are compared with existing approaches. Leveraging the Neyman-Pearson criterion, we derive expressions for the channel access probability, success probability, and mean achievable throughput of both networks while maintaining a fixed probability of false alarm. Approximations in the analytical results are validated through extensive simulations that demonstrate their accuracy.

INDEX TERMS Unmanned aerial vehicle network, spectrum sensing, spectrum sharing, cognitive radio network, success probability, throughput, stochastic geometry.

I. INTRODUCTION

A. BACKGROUND

Unmanned aerial vehicles (UAVs) have garnered significant attention in both academia and industry due to their mobility, flexibility, adjustable altitude, and symmetric maneuverability. With the evolution of cellular technology, UAVs are expected to serve as vital components in future networks, including sixth-generation (6G) and beyond 6G (B6G) wireless systems. UAV-assisted cellular networks are expected to enable a wide range of applications in future three-dimensional (3D) wireless systems, thereby posing new challenges [1]. For instance, aerial delivery systems require ultra-reliable, low-latency communication (URLLC) in 3D space for real-time navigation, fleet coordination, and status updates. Moreover, UAVs acting as aerial base stations (BSs) can complement terrestrial infrastructure in both small- and large-scale deployments. UAVs can be deployed rapidly and flexibly to provide network coverage for post-disaster recovery or in localized areas where temporary hotspots (e.g., concerts) are needed. In addition, UAVs can enhance signal coverage in areas with poor connectivity, such as cell-edge regions, as demonstrated in [2] and [3].

Meanwhile, as cellular networks evolve toward greater heterogeneity and face ever-increasing data demand, mobile operators are experiencing a critical challenge of spectrum scarcity. Spectrum sharing remains a viable solution for improving spectrum utilization and is expected to continue in 6G and B6G networks [4], [5]. While spectrum sharing has been extensively studied in terrestrial networks (TNs) through cognitive radio paradigms [6], [7], its application in 3D UAV networks is gaining increasing attention. Moreover, recent advancements in integrated sensing and communication (ISAC) have positioned UAVs as promising spectrum-aware agents capable of detecting spectral activity over wide geographic areas [8].

B. MOTIVATION AND RELATED WORK

In light of the aforementioned issues and the need for higher spectrum utilization, this work addresses a large-scale UAV-enabled spectrum sensing-based sharing system. In this

TABLE 1. Notation Table.

Parameter	Definition
$\Psi_{\rm g}$ and $\lambda_{\rm g}$	Point process of GBSs with density $\lambda_{\rm g}$
$\Psi_{\rm u}$ and $\lambda_{\rm u}$	Point process of the ground projection points of UAVs with density $\lambda_{\rm u}$
$h_{\rm u}$	Common altitude of the UAVs
$\widetilde{\Psi}_{\rm u}$	Point process of active UAVs
$R_{\rm s}$	Spectrum-sensing range
$R_{\rm d}$	Radius of the sensing disk on the ground plane
$b_x(r)$	Disk of radius r centered at x
$\|x-y\|$	Euclidean distance between nodes x and y
$\zeta(\theta)$	Probability of LoS for elevation angle θ
Ω	Channel power gain
Δ_θ	Bernoulli random variable indicating whether a link is LoS or NLoS
o	Origin (0,0)
$\Xi_{\rm g}$, $\Xi_{\rm u}$	SINR of the typical GBS user and typical UAV user
$I_{\rm g}$, $I_{\rm u}$	Aggregate interference power from the GBS and UAV networks to the typical GBS user
$\hat{I}_{\rm g}$, $\hat{I}_{\rm u}$	Aggregate interference power from the GBS and UAV networks to the typical UAV user
$P_{\rm g}$	GBS transmit power
$P_{\rm u}$	UAV transmit power
$\sigma_{\rm n}^2$	Noise power
$\mathcal{H}_0$, $\mathcal{H}_1$	Null and alternative hypothesis, respectively
$\Psi_{\rm g}(\mathcal{D})$	Cardinality of $\Psi_{\rm g}\cap\mathcal{D}$
β	Detection threshold for spectrum sensing
$p_{\rm f}$	Probability of false alarm
$p_{\rm m}$	Probability of missed detection
$p_{\rm e}$	Probability of total error
$\mathcal{L}_X(s)$	Laplace transforms of the random variable X evaluated at s
$\approx_d$	Approximate equality in distribution
$\kappa_{X,n}$	n-th cumulant of the random variable X
γ	Channel access probability based on spectrum sensing
$p_{\rm tx}$	Channel access probability for a GBS based on dynamic scheduling
$p_{\rm c,g}$, $p_{\rm c,u}$	Downlink success probabilities of the typical GBS user and the typical UAV user, respectively
η	Target SINR threshold for successful decoding
$\mathcal{C}_{\rm g}$, $\mathcal{C}_{\rm u}$	Throughputs of the GBS and UAV networks, respectively

model, UAVs act as aerial BSs of the secondary network and dynamically sense the spectrum usage of a terrestrial primary BS network, reusing it when it is available. Unlike cooperative or infrastructure-assisted models, our framework considers a fully decentralized UAV network. The proposed framework provides new insights into enabling scalable and spectrum-efficient UAV networks that intelligently coexist with terrestrial systems.

Several prior studies have investigated spectrum sensing and spectrum sharing in wireless networks, primarily focusing on terrestrial environments [9]–[14]. For instance, [9] evaluated interference bounds in an underlay cognitive radio network using the Poisson hole process (PHP) and Poisson cluster models under perfect sensing assumptions. In [10], small cell users opportunistically shared the uplink spectrum with macrocell users, modeled as a cognitive secondary network. Device-to-device (D2D) communication with sensing-based spectrum sharing was studied in [11] and [12]. In [11], sensing performance and network throughput were evaluated, while [12] extended the Poisson hole process (PHP)-based interference analysis from [14] to obtain approximate network performance. Similar to the analysis of terrestrial networks (TNs) using a 2D PHP, the work in [15] studies spectrum sharing in satellite–terrestrial integrated networks using a spherical PHP. Moreover, [16]–[18] analyze interference in coexisting TNs and non-terrestrial networks (NTNs). Specifically, [16] considers an NTN operating on a high-altitude platform (HAP), where base stations follow a PPP on a curved surface; [17] assumes that NTN base stations follow a spherical PPP at low Earth orbit (LEO) and share spectrum with TNs, investigating both uplink and downlink scenarios; and [18] studies a coexisting TN and satellite system targeting ground users in the S-band frequency under two different cases. Moreover, reference [19] studied the NOMA-based cognitive UAV in edge computing, optimizing the processing delay.

In contrast, relatively few studies have examined spectrum sensing and sharing in UAV-enabled networks, particularly in large-scale or 3D deployments. Reference [20] investigated UAV-ground spectrum sharing in mesh networks for disaster response. Both overlay and underlay sharing schemes were explored in [21], whereas [22] focused on optimizing drone-cell densities for underlay access. On the spectrum sensing front, [23], [24] addressed 3D sensing techniques. Reference [23] proposed a power control scheme based on real-time spectrum sensing to enhance spectrum reuse. In [24], which has a similar objective to our work, a machine learning-assisted stochastic geometry framework was employed to study the received signal power in D2D and UAV-based communications, using the same sensing technique as in [10]–[12]. We have shown in [25] that resorting to a learning-based approach is unnecessary since an exact characterization of the received signal power in such a UAV-based wireless network is possible.

While these works provide valuable insights into spectrum sensing and sharing, they primarily rely on approximation-based or learning-based methods. Motivated by the work of [24], we consider a sensing-based UAV-enabled network and develop a tractable and exact analytical framework to characterize the sensing performance.

C. CONTRIBUTIONS

The key contributions of this paper are summarized as follows:

- We develop a tractable stochastic-geometry-based framework to characterize spectrum sensing performance in large-scale UAV-enabled cellular networks. In particular, we derive expressions for the probabilities of false alarm and missed detection at the typical UAV, enabling a rigorous evaluation of sensing reliability under spatial randomness.
- Unlike prior works such as [10]–[12], [24], which rely on Gaussian approximations, i.i.d. sampling assumptions, or learning-based models, we provide an explicit characterization of the aggregate received signal power. This leads to a more accurate and analytically tractable evaluation of sensing performance.
- Leveraging a log-normal approximation of the aggregate received signal power, we derive a closed-form expression for the Neyman-Pearson detection threshold that satisfies a prescribed probability of false alarm. This result provides a practical design guideline for selecting the sensing threshold under a prescribed false alarm constraint.
- We analyze the computational complexity of the proposed sensing framework and compare it with that of existing methods. The results show that the proposed approach avoids the additional nested integrations required in prior works, leading to improved computational efficiency and enabling the feasible evaluation of exact mathematical expressions. In particular, we derive the first and second cumulants of the received signal power for the schemes in [10]–[12], [24], which were previously considered analytically intractable in [24] for a UAV-enabled network.
- Considering imperfect spectrum sensing, we characterize the channel access probability and evaluate network performance in terms of transmission success probability and throughput under a prescribed false alarm constraint. We further evaluate the joint success probability and joint throughput of the typical users in the primary and secondary networks, providing insights into how sensing errors impact system performance.
- We validate the approximations made in the analytical results through extensive Monte Carlo simulations of the sensing errors and the performance of both GBS and UAV networks.

II. SYSTEM MODEL

We consider a large-scale downlink cellular network comprising primary and secondary networks, as shown in Fig. 1, where the secondary network opportunistically accesses the licensed spectrum band. In 6G and beyond, such a secondary network that opportunistically shares spectrum to provide coverage to users can be particularly useful in scenarios where users require small data packets, intermittent transmissions, and can tolerate delays. For example, Internet of Things (IoT) devices that monitor environmental conditions such as temperature and pollution fall into this category. Smart meters for water, gas, and electricity provide another relevant example.

A. NETWORK ARCHITECTURE AND SPATIAL MODELING

The primary network consists of GBSs and their associated users, whereas the secondary network comprises UAVs acting as aerial BSs along with their users. Furthermore, each BS serves only the users within its own network and operates identically to the other BSs in that network.

The locations of GBSs are modeled as a homogeneous Poisson point process (PPP) $\Psi_{\mathrm{g}} \triangleq \{x_1, x_2, ...\} \subset \mathbb{R}^2$ with density λ_{g}. Similarly, the ground projection points of the UAVs are modeled as another independent homogeneous PPP $\Psi_{\mathrm{u}} \triangleq \{y_1, y_2, \ldots\} \subset \mathbb{R}^2$ with density λ_{u}. All UAVs hover at a common altitude $h_{\mathrm{u}} \in \mathbb{R}_+$,[1] yielding UAV coordinates in $\mathbb{R}^2 \times \mathbb{R}_+$, where (y, h_{u}), $y \in \Psi_{\mathrm{u}}$. The GBSs and users are assumed to be located on the ground plane; hence, altitude variations are neglected.

Each UAV performs spectrum sensing to determine whether the licensed spectrum is occupied by nearby GBSs. Based on the sensing outcome, UAVs that identify spectrum holes are permitted to access the licensed spectrum while minimizing interference to the downlink transmissions of GBSs. The objective of sensing is to detect the presence of GBSs within a spectrum-sensing region. For instance, we consider the typical UAV with its ground projection located at y_{s}, conditioned on $y_{\mathrm{s}} \in \Psi_{\mathrm{u}}$, which will be used in all equations and analyses for evaluating the performance of spectrum sensing.[2] Since GBSs are located on the ground, for the typical UAV, the intersection of its 3D sensing ball of radius R_{s} with the ground plane forms a disk $\mathcal{D} = b_{y_{\mathrm{s}}}(R_{\mathrm{d}})$, where $R_{\mathrm{d}} = \sqrt{R_{\mathrm{s}}^2 - h_{\mathrm{u}}^2}$ and $b_x(r)$ denotes a disk of radius r centered at x.

Finally, based on the sensing outcomes, the UAVs that detect spectrum holes are allowed to share the licensed spectrum. The set of such UAVs is denoted by $\widetilde{\Psi}_{\mathrm{u}}$, where $\widetilde{\Psi}_{\mathrm{u}} \subset \Psi_{\mathrm{u}}$.

B. CHANNEL MODELING

We adopt a standard path-loss model $\|x - y\|^{-\alpha}$, where $\|x - y\|$ denotes the Euclidean distance between nodes x and y in $\mathbb{R}^n$, where $n \in \{2, 3\}$. The path-loss exponent α is defined as $\alpha \in \{\alpha_{\mathrm{g}}, \alpha_{\mathrm{u}}\}$, where α_{g} denotes the exponent for ground-to-ground links, and α_{u} denotes that for ground-to-air links. A wireless channel can be classified as LoS or non-

[1] Practically, UAVs may hover based on network requirements. Specifically, when UAVs operate as aerial BSs to provide coverage to ground users within a finite area, they hover at the same altitude; however, the altitude may vary due to factors such as their control systems and wind speed.

[2] Note that conditioning on a point at a specific location is equivalent to adding a point in a PPP. According to Slivnyak's theorem [26], such conditioning does not alter the distribution of the other points.

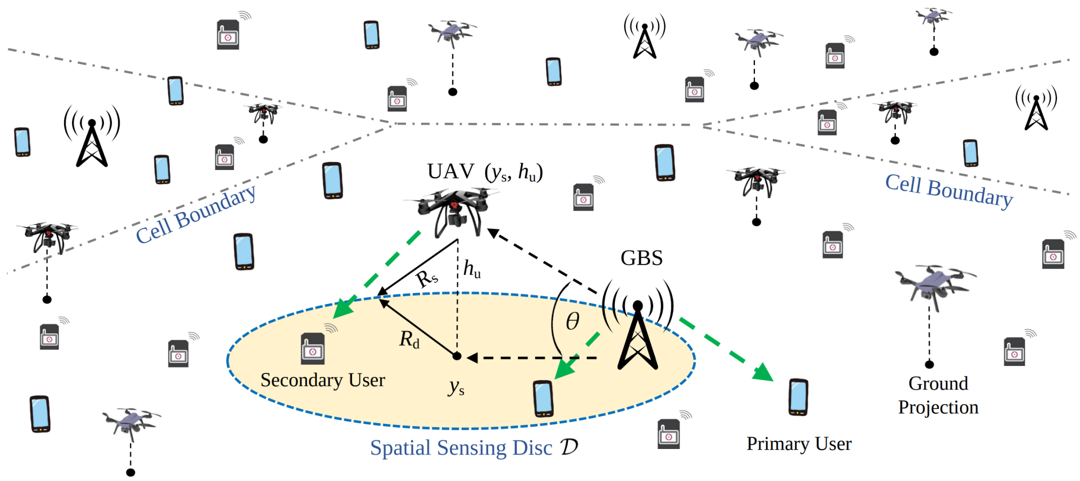

FIGURE 1. The proposed system model illustrates spectrum sensing in a UAV-assisted cellular network.

line-of-sight (NLoS), depending on whether there is a direct visual path between the transmitter and the receiver. Due to their altitude, UAVs may experience either LoS or NLoS propagation conditions. The probability of a LoS channel is modeled as a function of the elevation angle, as given in [27]:

$$\zeta(\theta) = \frac{1}{1 + c_2 \exp(-c_1 \theta)}, \tag{1}$$

where θ is the elevation angle, c_1 and c_2 are environment-dependent constants (e.g., rural, urban). Since the elevation angle is negligible, we model all ground-to-ground links as NLoS.

We adopt a Nakagami-m fading model for small-scale fading, where the channel power gain Ω follows the gamma distribution: $\Omega \sim \mathrm{Gamma}(m, m)$ with shape and rate parameters both equal to $m > 0$. The mean and variance of Ω are 1 and $\frac{1}{m}$, respectively. For ground-to-air links, two fading models are considered:

1) **LoS Channel:** For LoS channel, $m = \frac{(K+1)^2}{2K+1}$, where K is the Rician K-factor representing the ratio of the power in the LoS component to that in the scattered components.
2) **NLoS Channel:** For NLoS channel, $m = 1$, due to the absence of a strong LoS path.

Based on the LoS probability, we define a Bernoulli random variable $\Delta_\theta \in \{0, 1\}$, where $\mathbb{P}(\Delta_\theta = 1) = \zeta(\theta)$ denotes the probability of a LoS channel. The variable Δ_θ determines the fading channel type as

$$\Delta_\theta = \begin{cases} 1, & \text{LoS} \\ 0, & \text{NLoS}. \end{cases} \tag{2}$$

The composite channel power gain for ground-to-air links is modeled as

$$\widetilde{\Omega}_{\mathrm{u}} \triangleq \Delta_\theta \Omega_{\mathrm{u}}^{\mathrm{L}} + (1 - \Delta_\theta)\Omega_{\mathrm{u}}^{\mathrm{N}}, \tag{3}$$

where $\Omega_{\mathrm{u}}^{\mathrm{L}} \sim \mathrm{Gamma}(m, m)$ with $m > 1$ represents the LoS channel power gain, and $\Omega_{\mathrm{u}}^{\mathrm{N}} \sim \mathrm{Exp}(1)$ represents the NLoS channel power gain.

C. USER ASSOCIATION AND SINR MODEL

Without loss of generality, we assume that the typical GBS user is located at the origin, $o \triangleq (0, 0) \in \mathbb{R}^2$, and the typical UAV user is located at $z \in \mathbb{R}^2$. Users in both networks associate with the BS in their respective network that provides the highest average received signal power.[3] The nearest GBS provides the strongest average received signal power to the typical GBS user, which is defined as

$$x_o = \arg\min_{x \in \Psi_{\mathrm{g}}} \|x\|. \tag{4}$$

Similarly, the typical UAV user is also associated with the nearest UAV (y_z, h_{u}), i.e.,

$$y_z = \arg\min_{y \in \widetilde{\Psi}_{\mathrm{u}}} \|z - y\|. \tag{5}$$

The signal-to-interference-plus-noise ratio (SINR) of the typical GBS user is

$$\Xi_{\mathrm{g},o} \triangleq \frac{P_{\mathrm{g}} r_{\mathrm{g}}^{-\alpha_{\mathrm{g}}} \Omega_{\mathrm{g},o}^{\mathrm{N}}}{I_{\mathrm{g}} + I_{\mathrm{u}} + \sigma_{\mathrm{n}}^2}, \tag{6}$$

where P_{g} is the GBS transmit power, r_{g} denotes the distance between the typical GBS user and the serving GBS x_o, σ_{n}^2 denotes noise power, $\Omega_{\mathrm{g},o}^{\mathrm{N}}$ is the channel power gain from the serving GBS x_o, and I_{g} and I_{u} represent the aggregate interference powers from the GBS and UAV networks, respectively:

$$I_{\mathrm{g}} \triangleq \sum_{x \in \Psi_{\mathrm{g}} \setminus x_o} P_{\mathrm{g}} \|x\|^{-\alpha_{\mathrm{g}}} \Omega_{\mathrm{g},x}^{\mathrm{N}}, \tag{7}$$

$$I_{\mathrm{u}} \triangleq \sum_{y \in \widetilde{\Psi}_{\mathrm{u}}} P_{\mathrm{u}} \left(\|y\|^2 + h_{\mathrm{u}}^2\right)^{-\frac{\alpha_{\mathrm{u}}}{2}} \widetilde{\Omega}_{\mathrm{u},y}, \tag{8}$$

where $\Omega_{\mathrm{g},x}^{\mathrm{N}}$ and $\widetilde{\Omega}_{\mathrm{u},y}$ are channel power gains from GBS x and UAV y.

[3]Once an active UAV begins sharing the spectrum, it suspends spectrum sensing for a predetermined period. To reduce signaling overhead and avoid frequent handovers, each UAV performs spectrum sensing at regular intervals, the duration of which depends on the activity period of a GBS.

The SINR of the typical UAV user is

$$\Xi_{\mathrm{u},z} \triangleq \frac{P_{\mathrm{u}}\left(r_{\mathrm{u}}^2+h_{\mathrm{u}}^2\right)^{-\frac{\alpha_{\mathrm{u}}}{2}} \widetilde{\Omega}_{\mathrm{u},y_z}}{\hat{I}_{\mathrm{g}}+\hat{I}_{\mathrm{u}}+\sigma_{\mathrm{n}}^2}, \quad z \in \mathbb{R}^2, \tag{9}$$

where P_{u} is the UAV transmit power, r_{u} denotes the distance between the typical UAV user and the projection point of the serving UAV (y_z, h_{u}), $\widetilde{\Omega}_{\mathrm{u},y_z}$ is the channel power gain associated with the serving UAV. The aggregate interference powers from the GBS and UAV networks are given by

$$\hat{I}_{\mathrm{g}} \triangleq \sum_{x\in\Psi_{\mathrm{g}}} P_{\mathrm{g}}\|x\|^{-\alpha_{\mathrm{g}}}\Omega_{\mathrm{g},x}^{\mathrm{N}}, \tag{10}$$

$$\hat{I}_{\mathrm{u}} \triangleq \sum_{y\in\widetilde{\Psi}_{\mathrm{u}}\backslash y_z} P_{\mathrm{u}}\left(\|y\|^2+h_{\mathrm{u}}^2\right)^{-\frac{\alpha_{\mathrm{u}}}{2}} \widetilde{\Omega}_{\mathrm{u},y}. \tag{11}$$

D. SPECTRUM SENSING AND HYPOTHESIS TESTING

Each UAV evaluates the signal power of a licensed spectrum band to determine whether it is accessible. Leveraging an energy detection scheme, all UAVs sense the spectrum during the spectrum sensing period. After a sufficiently long sensing duration, the effects of small-scale fading are averaged out, and the required sensing duration depends on the channel coherence time and the variance of the fading process. Every UAV $(y, h_{\mathrm{u}}), y \in \Psi_{\mathrm{u}}$ measures the total received signal power T_y, given by

$$T_y = \sum_{x\in\Psi_{\mathrm{g}}} P_{\mathrm{g}}\|(y,h_{\mathrm{u}})-(x,0)\|^{-\alpha_{\mathrm{u}}}+\sigma_{\mathrm{n}}^2. \tag{12}$$

The spectrum sensing problem for the typical UAV is modeled as a binary hypothesis test: $\mathcal{H}_0$ and $\mathcal{H}_1$ [28]. The null hypothesis $\mathcal{H}_0$ corresponds to the absence of GBSs within the sensing region $\mathcal{D}$ (i.e., a spectrum hole), while the alternative hypothesis $\mathcal{H}_1$ corresponds to the presence of at least one GBS in $\mathcal{D}$. Formally:

$$\begin{cases}\mathcal{H}_0 : \Psi_{\mathrm{g}}(\mathcal{D}) = 0\\ \mathcal{H}_1 : \Psi_{\mathrm{g}}(\mathcal{D}) \neq 0\end{cases}. \tag{13}$$

III. SPECTRUM SENSING AND NETWORK PERFORMANCE

In this section, we investigate the spectrum sensing performance of the proposed wireless network in terms of the probability of false alarm and the probability of missed detection. Building on the imperfect sensing outcomes, we characterize the deployment of secondary BSs and evaluate the resulting network performance.

A. ERROR IN SPECTRUM SENSING

To determine channel access, the typical UAV $(y_{\mathrm{s}}, h_{\mathrm{u}})$ compares the measured received signal power against a detection threshold β, i.e.,

$$T_{y_{\mathrm{s}}} \underset{\mathcal{H}_1}{\overset{\mathcal{H}_0}{\lessgtr}} \beta, \tag{14}$$

where $T_{y_{\mathrm{s}}}$ is defined in (12). With this imperfect spectrum sensing, the set of active UAVs can be expressed as

$$\widetilde{\Psi}_{\mathrm{u}} \triangleq \{y \in \Psi_{\mathrm{u}} : T_y < \beta\}. \tag{15}$$

The probability of false alarm is defined as

$$p_{\mathrm{f}} \triangleq \mathbb{P}\left(T_{y_{\mathrm{s}}} > \beta \mid \Psi_{\mathrm{g}}(\mathcal{D}) = 0\right). \tag{16}$$

Similarly, the probability of missed detection is

$$p_{\mathrm{m}} \triangleq \mathbb{P}\left(T_{y_{\mathrm{s}}} < \beta \mid \Psi_{\mathrm{g}}(\mathcal{D}) \neq 0\right). \tag{17}$$

Moreover, the probability of total error can be found using the law of total probability:

$$p_{\mathrm{e}} = p_{\mathrm{f}}\mathbb{P}(\Psi_{\mathrm{g}}(\mathcal{D})=0)+p_{\mathrm{m}}\mathbb{P}(\Psi_{\mathrm{g}}(\mathcal{D})\neq 0), \tag{18}$$

where

$$\mathbb{P}(\Psi_{\mathrm{g}}(\mathcal{D})=0) = \exp\left(-\pi\lambda_{\mathrm{g}}(R_{\mathrm{s}}^2-h_{\mathrm{u}}^2)\right), \tag{19}$$

$$\mathbb{P}(\Psi_{\mathrm{g}}(\mathcal{D})\neq 0) = 1-\exp\left(-\pi\lambda_{\mathrm{g}}(R_{\mathrm{s}}^2-h_{\mathrm{u}}^2)\right). \tag{20}$$

To simplify the analysis, we define a scale-transformed random variable

$$\widetilde{T} = \frac{T_{y_{\mathrm{s}}}-\sigma_{\mathrm{n}}^2}{P_{\mathrm{g}}}. \tag{21}$$

The random variable $\widetilde{T}$ is defined without conditioning on the sensing event. Based on this, we define

$$\widetilde{T}_0 = \left(\widetilde{T} \mid \Psi_{\mathrm{g}}(\mathcal{D})=0\right), \tag{22}$$

$$\widetilde{T}_1 = \left(\widetilde{T} \mid \Psi_{\mathrm{g}}(\mathcal{D})\neq 0\right). \tag{23}$$

Accordingly, the probabilities of false alarm and missed detection can be expressed as

$$p_{\mathrm{f}} = \bar{F}_{\widetilde{T}_0}\left(\frac{\beta-\sigma_{\mathrm{n}}^2}{P_{\mathrm{g}}}\right), \quad p_{\mathrm{m}} = F_{\widetilde{T}_1}\left(\frac{\beta-\sigma_{\mathrm{n}}^2}{P_{\mathrm{g}}}\right),$$

where $\beta > \sigma_{\mathrm{n}}^2$, and F_Z and $\bar{F}_Z$ denote the cumulative distribution function (CDF) and complementary CDF (CCDF) of the random variable Z, respectively.

Theorem 1. *The Laplace transforms of the random variables $\widetilde{T}_0$ and $\widetilde{T}_1$ defined in* (22) *and* (23)*, respectively, for a given sensing range R_{s} and UAV altitude h_{u}, are given by*

$$\mathcal{L}_{\widetilde{T}_0}(s) = \exp\left(-\pi\lambda_{\mathrm{g}}\phi(s,R_{\mathrm{s}}^2)\right), \tag{24}$$

$$\mathcal{L}_{\widetilde{T}_1}(s) = \frac{\exp\left(-\pi\lambda_{\mathrm{g}}\phi(s,h_{\mathrm{u}}^2)\right)}{1-\exp\left(-\pi\lambda_{\mathrm{g}}(R_{\mathrm{s}}^2-h_{\mathrm{u}}^2)\right)} - \frac{\mathcal{L}_{\widetilde{T}_0}(s)}{\exp\left(\pi\lambda_{\mathrm{g}}(R_{\mathrm{s}}^2-h_{\mathrm{u}}^2)\right)-1}, \tag{25}$$

where $a, b \in \mathbb{R}_+$, $\phi(a,b)$ is defined as

$$\begin{aligned}\phi(a,b) &= \int_b^\infty \left\{1-\exp\left(-av^{-\frac{\alpha_{\mathrm{u}}}{2}}\right)\right\}\mathrm{d}v\\ &= a^{\frac{2}{\alpha_{\mathrm{u}}}}\Gamma\left(1-\frac{2}{\alpha_{\mathrm{u}}}\right)-\int_0^b 1-\exp\left(-av^{-\frac{\alpha_{\mathrm{u}}}{2}}\right)\mathrm{d}v,\end{aligned}$$

and $\Gamma(a) = \int_0^\infty v^{a-1}e^{-v}\mathrm{d}v$ denotes the gamma function.

Proof:
See Appendix A. ∎

For a non-negative random variable Z, its probability density function (PDF) can be obtained via the inverse Laplace transform:

$$f_Z(z) = \mathcal{L}^{-1}\{\mathcal{L}_Z(s)\}(z), \quad s > 0. \tag{26}$$

Therefore, the PDF of $\widetilde{T}_0$ is:

$$\begin{aligned} f_{\widetilde{T}_0}(\tau) =& \mathcal{L}^{-1}\left\{\mathcal{L}_{\widetilde{T}_0}(s)\right\}(\tau) \\ =& \mathcal{L}^{-1}\left[\exp\left(-\pi\lambda_{\mathrm{g}}\phi(s,R_{\mathrm{s}}^2)\right)\right](\tau). \end{aligned} \tag{27}$$

This result must be evaluated numerically since a closed-form inverse Laplace transform is not available. The inverse Laplace transform can be computed efficiently using the Euler algorithm, as shown in [29].

Similarly, the PDF of $\widetilde{T}_1$ is:

$$\begin{aligned} f_{\widetilde{T}_1}(\tau) =& \frac{\mathcal{L}^{-1}\left[\exp\left(-\pi\lambda_{\mathrm{g}}\phi(s,h_{\mathrm{u}}^2)\right)\right](\tau)}{1-\exp\left(-\pi\lambda_{\mathrm{g}}(R_{\mathrm{s}}^2-h_{\mathrm{u}}^2)\right)} - \\ & \frac{f_{\widetilde{T}_0}(\tau)}{\exp\left(\pi\lambda_{\mathrm{g}}(R_{\mathrm{s}}^2-h_{\mathrm{u}}^2)\right)-1}. \end{aligned} \tag{28}$$

Theorem 2. *For a sensing range R_{s} and UAV altitude h_{u}, the probabilities of false alarm and missed detection are*

$$p_{\mathrm{f}} = 1-\mathcal{L}^{-1}\left[\frac{1}{s}\exp\left(-\pi\lambda_{\mathrm{g}}\phi(s,R_{\mathrm{s}}^2)\right)\right](\tau)\bigg|_{\tau=\frac{\beta-\sigma_{\mathrm{n}}^2}{P_{\mathrm{g}}}}, \tag{29}$$

$$\begin{aligned} p_{\mathrm{m}} =& \frac{\mathcal{L}^{-1}\left[\frac{1}{s}\exp\left(-\pi\lambda_{\mathrm{g}}\phi(s,h_{\mathrm{u}}^2)\right)\right](\tau)\Big|_{\tau=\frac{\beta-\sigma_{\mathrm{n}}^2}{P_{\mathrm{g}}}}}{1-\exp\left(-\pi\lambda_{\mathrm{g}}(R_{\mathrm{s}}^2-h_{\mathrm{u}}^2)\right)} - \\ & \frac{1-p_{\mathrm{f}}}{\exp\left(\pi\lambda_{\mathrm{g}}(R_{\mathrm{s}}^2-h_{\mathrm{u}}^2)\right)-1}. \end{aligned} \tag{30}$$

Proof:
For a non-negative random variable Z, its CDF is given by $F_Z(z) = \mathcal{L}^{-1}\left\{\frac{1}{s}\mathcal{L}_Z(s)\right\}(z)$. Applying this property to Theorem 1 yields the result. ■

Corollary 1. *For a sensing range R_{s} and UAV altitude h_{u}, the total error probability is*

$$\begin{aligned} p_{\mathrm{e}} =& \mathcal{L}^{-1}\left\{\frac{1}{s}\exp\left(-\pi\lambda_{\mathrm{g}}\phi(s,h_{\mathrm{u}}^2)\right)\right\}(\tau)\bigg|_{\tau=\frac{\beta-\sigma_{\mathrm{n}}^2}{P_{\mathrm{g}}}} - \\ & \frac{(1-2p_{\mathrm{f}})}{\exp\left(\pi\lambda_{\mathrm{g}}(R_{\mathrm{s}}^2-h_{\mathrm{u}}^2)\right)-1}. \end{aligned} \tag{31}$$

Proof:
The result follows by substituting p_{f} and p_{m} from Theorem 2 together with (19) and (20) into (18). ■

B. NEYMAN–PEARSON DETECTOR

According to the Neyman-Pearson criterion, fixing one error probability (either the probability of false alarm or the probability of missed detection), the other can be minimized. The analytical results in Theorem 2 are numerically tractable, but closed-form expressions are unavailable. To overcome this limitation, we use an approximation based on a log-normal distribution of the random variable $\widetilde{T}_0$ defined in (22) to determine the Neyman-Pearson detection threshold for a given probability of false alarm.

Lemma 1. *For the spectrum sensing range R_{s}, the random variable $\widetilde{T}_0$ can be approximated by a log-normal distribution as*

$$\ln\left(\widetilde{T}_0\right) \approx_d \mathcal{N}\left(\ln\left[\frac{\kappa_1}{\sqrt{c}}\right], \ln c\right), \tag{32}$$

where $c = \frac{\kappa_2}{\kappa_1^2}+1$, and the n-th cumulant of the random variable $\widetilde{T}_0$ is given by

$$\kappa_n = \frac{2\pi\lambda_{\mathrm{g}}R_{\mathrm{s}}^{2-n\alpha_{\mathrm{u}}}}{n\alpha_{\mathrm{u}}-2}, \quad n\in\mathbb{N},\ \alpha_{\mathrm{u}}>2. \tag{33}$$

Proof:
The distribution of the received signal power at the typical UAV can be approximated by a log-normal distribution when the GBSs form a homogeneous PPP [30]. Consequently, $\widetilde{T}_0$ defined in (22) can be approximated as a log-normal random variable as

$$\ln\left(\widetilde{T}_0\right) \approx_d \mathcal{N}\left(\mu_0,\sigma_0^2\right), \tag{34}$$

where $\approx_d$ denotes the approximate equality in distribution. Using the Laplace transform from (24), the n-th cumulant of $\widetilde{T}_0$ is computed as

$$\begin{aligned} \kappa_n &= (-1)^n\frac{\mathrm{d}^n}{\mathrm{d}s^n}\ln\mathcal{L}_{\widetilde{T}_0}(s)\Big|_{s=0} = \pi\lambda_{\mathrm{g}}\int_{R_{\mathrm{s}}^2}^{\infty} y^{-n\frac{\alpha_{\mathrm{u}}}{2}}\mathrm{d}y \\ &= \frac{2\pi\lambda_{\mathrm{g}}R_{\mathrm{s}}^{2-n\alpha_{\mathrm{u}}}}{n\alpha_{\mathrm{u}}-2}. \end{aligned} \tag{35}$$

Then, using the first and second cumulants,

$$\mu_0 = \ln\left(\frac{\kappa_1}{\sqrt{\frac{\kappa_2}{\kappa_1^2}+1}}\right), \quad \sigma_0^2 = \ln\left(\frac{\kappa_2}{\kappa_1^2}+1\right).$$

■

Theorem 3. *Based on the log-normal approximation of the received signal power, for a given sensing range R_{s}, the sensing threshold β^* for a Neyman-Pearson detector with a specified probability of false alarm p_{f}^* is given by*

$$\beta^* = \sigma_{\mathrm{n}}^2 + \frac{P_{\mathrm{g}}\kappa_1}{\sqrt{c}}\exp\left(\sqrt{2\ln c}\,\mathrm{erfc}^{-1}(2p_{\mathrm{f}}^*)\right), \tag{36}$$

where $\mathrm{erfc}^{-1}(\cdot)$ is the inverse complementary error function.

Proof:
From Lemma 1 and the definition of the probability of false alarm in (16):

$$\begin{aligned} p_{\mathrm{f}} &= 1-\frac{1}{2}\left[1+\mathrm{erf}\left(\frac{\ln\left(\frac{\beta-\sigma_{\mathrm{n}}^2}{P_{\mathrm{g}}}\right)-\mu_0}{\sigma_0\sqrt{2}}\right)\right] \\ &= \frac{1}{2}\mathrm{erfc}\left[\frac{\ln\left(\frac{\beta-\sigma_{\mathrm{n}}^2}{P_{\mathrm{g}}}\right)-\mu_0}{\left(\sigma_0\sqrt{2}\right)}\right]. \end{aligned} \tag{37}$$

Solving this equation for a given probability of false alarm p_{f}^* yields the desired Neyman-Pearson threshold β^*. ■

C. COMPARISON BETWEEN THE PROPOSED SPECTRUM SENSING SCHEME AND THE SCHEME IN [10]–[12], [24]

We evaluate the sensing errors based on the scheme in [10]–[12], [24] for the system model in Fig. 1 and compare with our proposed scheme in terms of performance and complexity. In the spectrum sensing scheme of these prior articles, the sample received signals are assumed to be i.i.d., and the test statistic is approximated by a normal distribution, from which the probabilities of false alarm and missed detection are derived as

$$\begin{aligned} p_{\mathrm{f}} &= \mathbb{E}_{Z_0}\left[Q\left(\frac{\beta - Z_0 - \sigma_{\mathrm{n}}^2}{Z_0+\sigma_{\mathrm{n}}^2}\sqrt{N_{\mathrm{s}}}\right)\right] \\ &= \int_0^\infty Q\left(\frac{\beta - z - \sigma_{\mathrm{n}}^2}{z+\sigma_{\mathrm{n}}^2}\sqrt{N_{\mathrm{s}}}\right) f_{Z_0}(z)\mathrm{d}z, \end{aligned} \tag{38}$$

$$\begin{aligned} p_{\mathrm{m}} &= \frac{\mathbb{E}_Z\left[Q\left(\frac{\beta-Z-\sigma_{\mathrm{n}}^2}{Z+\sigma_{\mathrm{n}}^2}\sqrt{N_{\mathrm{s}}}\right)\right]}{1-e^{(-\pi\lambda_{\mathrm{g}}(R_{\mathrm{s}}^2-h_{\mathrm{u}}^2))}} - \frac{1-p_{\mathrm{f}}}{e^{(\pi\lambda_{\mathrm{g}}(R_{\mathrm{s}}^2-h_{\mathrm{u}}^2))}-1} \\ &= \frac{\int_0^\infty Q\left(\frac{\beta-z-\sigma_{\mathrm{n}}^2}{z+\sigma_{\mathrm{n}}^2}\sqrt{N_{\mathrm{s}}}\right) f_Z(z)\mathrm{d}z}{1-e^{(-\pi\lambda_{\mathrm{g}}(R_{\mathrm{s}}^2-h_{\mathrm{u}}^2))}} - \frac{1-p_{\mathrm{f}}}{e^{(\pi\lambda_{\mathrm{g}}(R_{\mathrm{s}}^2-h_{\mathrm{u}}^2))}-1}, \end{aligned} \tag{39}$$

where $Q(\cdot)$ is the Gaussian Q-function, $Z_0 = \sum_{\substack{x\in\Psi_{\mathrm{g}},\\ \Psi_{\mathrm{g}}(\mathcal{D})=0}} P_{\mathrm{g}}\Omega_{u,i}\|(y_{\mathrm{s}},h_{\mathrm{u}}) - (x,0)\|^{-\alpha_{\mathrm{u}}}$, and $Z = \sum_{x\in\Psi_{\mathrm{g}}} P_{\mathrm{g}}\Omega_{u,i}\|(y_{\mathrm{s}},h_{\mathrm{u}}) - (x,0)\|^{-\alpha_{\mathrm{u}}}$, f_{Z_0} denotes the PDF of Z_0, f_Z denotes the PDF of Z, and N_{s} denotes the number of samples.

Following the derivation of Theorem 1 and (27), the PDFs of Z_0 and Z are obtained. Note that in (12), the channel power fading gain is not included due to the averaging over a number of received signal samples during spectrum sensing. In contrast, Z_0 and Z incorporate the channel fading gain, consistent with the spectrum sensing scheme in [10]–[12], [24]. Unlike the channel model in [24], where LoS and NLoS channels are treated similarly by applying an attenuation factor for NLoS links, our model explicitly separates LoS and NLoS channels. Based on the channel model described in (3), following similar derivation of Theorem 1, and letting the elevation angle $\theta = \tan^{-1}\frac{h_{\mathrm{u}}}{x}$, where x denotes the horizontal distance between the UAV's ground projection and a ground node, the Laplace transforms of Z_0 and Z are derived as follows:

$$\begin{aligned} \mathcal{L}_{Z_0}(s) &= \exp\left(-\pi\lambda_{\mathrm{g}}\int_{R_{\mathrm{s}}^2}^\infty\left\{1-\mathbb{E}\left[e^{\left(-\frac{sP_{\mathrm{g}}\tilde{\Omega}_{\mathrm{u}}}{v^{\frac{\alpha_{\mathrm{u}}}{2}}}\right)}\right]\right\}\mathrm{d}v\right) \\ &= \exp\left(-\pi\lambda_{\mathrm{g}}\int_{R_{\mathrm{s}}^2}^\infty\left\{1-\zeta\left(\sin^{-1}\frac{h_{\mathrm{u}}}{\sqrt{v}}\right)\mathcal{L}_{\Omega_{\mathrm{u}}^{\mathrm{L}}}\left(sP_{\mathrm{g}}v^{-\frac{\alpha_{\mathrm{u}}}{2}}\right)\right.\right. \\ &\quad \left.\left. -\left[1-\zeta\left(\sin^{-1}\frac{h_{\mathrm{u}}}{\sqrt{v}}\right)\right]\mathcal{L}_{\Omega_{\mathrm{u}}^{\mathrm{N}}}\left(sP_{\mathrm{g}}v^{-\frac{\alpha_{\mathrm{u}}}{2}}\right)\right\}\mathrm{d}v\right), \end{aligned} \tag{40}$$

where $\mathcal{L}_{\Omega_{\mathrm{u}}^{\mathrm{L}}}(a) = \left(\frac{m}{m+a}\right)^m$ and $\mathcal{L}_{\Omega_{\mathrm{u}}^{\mathrm{N}}}(a) = \frac{1}{1+a}$ are the Laplace transforms of the LoS and NLoS fading channel power gains, respectively. Substituting these transforms, the Laplace transform of Z_0 is then expressed as:

$$\begin{aligned} \mathcal{L}_{Z_0}(s) &= \exp\left(-\pi\lambda_{\mathrm{g}}\int_{R_{\mathrm{s}}^2}^\infty\left\{\frac{sP_{\mathrm{g}}}{sP_{\mathrm{g}}+v^{\frac{\alpha_{\mathrm{u}}}{2}}} - \zeta\left(\sin^{-1}\frac{h_{\mathrm{u}}}{\sqrt{v}}\right)\right.\right. \\ &\quad \left.\left.\times\left[\left(1+\frac{sP_{\mathrm{g}}}{mv^{\frac{\alpha_{\mathrm{u}}}{2}}}\right)^{-m} - \frac{1}{1+sP_{\mathrm{g}}v^{-\frac{\alpha_{\mathrm{u}}}{2}}}\right]\right\}\mathrm{d}v\right). \end{aligned} \tag{41}$$

Using (26), the PDF of Z_0 can be expressed as

$$\begin{aligned} f_{Z_0}(z) &= \\ &\mathcal{L}^{-1}\left[\exp\left(-\pi\lambda_{\mathrm{g}}\int_{R_{\mathrm{s}}^2}^\infty\left\{\frac{sP_{\mathrm{g}}}{sP_{\mathrm{g}}+v^{\frac{\alpha_{\mathrm{u}}}{2}}} - \zeta\left(\sin^{-1}\frac{h_{\mathrm{u}}}{\sqrt{v}}\right)\right.\right.\right. \\ &\left.\left.\left.\times\left[\left(1+\frac{sP_{\mathrm{g}}}{mv^{\frac{\alpha_{\mathrm{u}}}{2}}}\right)^{-m} - \frac{1}{1+sP_{\mathrm{g}}v^{-\frac{\alpha_{\mathrm{u}}}{2}}}\right]\right\}\mathrm{d}v\right)\right](z). \end{aligned} \tag{42}$$

Similarly, the PDF of Z can be derived as

$$\begin{aligned} f_Z(z) &= \\ &\mathcal{L}^{-1}\left[\exp\left(-\pi\lambda_{\mathrm{g}}\int_{h_{\mathrm{u}}^2}^\infty\left\{\frac{sP_{\mathrm{g}}}{sP_{\mathrm{g}}+v^{\frac{\alpha_{\mathrm{u}}}{2}}} - \zeta\left(\sin^{-1}\frac{h_{\mathrm{u}}}{\sqrt{v}}\right)\right.\right.\right. \\ &\left.\left.\left.\times\left[\left(1+\frac{sP_{\mathrm{g}}}{mv^{\frac{\alpha_{\mathrm{u}}}{2}}}\right)^{-m} - \frac{1}{1+sP_{\mathrm{g}}v^{-\frac{\alpha_{\mathrm{u}}}{2}}}\right]\right\}\mathrm{d}v\right)\right](z). \end{aligned} \tag{43}$$

1) COMPLEXITY COMPARISON

The proposed spectrum sensing performance is presented in Theorem 2, which involves the inverse Laplace transform of a function $\phi(x,y)$. The function $\phi(x,y)$ itself is defined as an integral. Since neither the integral nor its inverse Laplace transform can be expressed in closed-form, numerical evaluation is necessary. In our numerical analysis, we employ the Euler algorithm–a sum-based method–for computing the inverse Laplace transform [29]. This method requires a summation over M terms, yielding a complexity of $\mathcal{O}(M)$. Additionally, the numerical integration of $\phi(x,y)$ has a complexity of $\mathcal{O}(L)$, where L denotes the number of function evaluations. The values of M and L determine the precision of the computation. Therefore, the overall complexity of computing p_{f} in Theorem 2 is $\mathcal{O}(ML)$. The probability of missed detection, p_{m}, in Theorem 2 consists of two components, each with the same complexity of $\mathcal{O}(ML)$. In our simulation, we chose $M = 32$, which provides sufficient precision. The value of L depends on the nature of the integrand; for example, a highly oscillatory function may require a larger L.

In contrast, the spectrum sensing scheme used in [10]–[12], [24] follows a similar computational approach. However, after applying the inverse Laplace transform to the integrand, an additional outer integral is required to compute the expectation of a random variable, as shown in (38) and (39), with complexity $\mathcal{O}(L_{\text{out}})$. Hence, the total complexity of p_{f} in (38) becomes $\mathcal{O}(L_{\text{out}}ML)$, and the expression for p_{m}

in (39) consists of two parts, each with the same complexity $\mathcal{O}(L_{\text{out}}ML)$. Because of this computational burden, exact analysis was deemed infeasible and an approximation was adopted by the authors of [10]–[12], [24].

2) SENSING PERFORMANCE COMPARISON

While [10]–[12] approximated the random variables representing the received signal power under conditions $\Psi_{\mathrm{g}}(\mathcal{D}) = 0$ and $\Psi_{\mathrm{g}}(\mathcal{D}) \neq 0$ by deriving the first and second cumulants, [24] employed a machine learning approach, claiming that cumulants cannot be evaluated due to the mixed LoS/NLoS channel modeling assumption. However, the first and second cumulants of the random variables representing the received signal power under the conditions can, in fact, be derived for networks where UAVs receive signals from GBSs. The Laplace transforms of Z_0 is given in (41). Following the proof of Lemma 1, the n-th cumulant of the random variable Z_0 can be expressed as

$$\begin{aligned}
\kappa_{Z_0,n} &= (-1)^n \frac{\mathrm{d}^n}{\mathrm{d}s^n} \ln \mathcal{L}_{Z_0}(s)\Big|_{s=0} \\
&= n!\pi\lambda_{\mathrm{g}} P_{\mathrm{g}}^n \int_{R_{\mathrm{s}}^2}^{\infty} v^{-\frac{n\alpha_{\mathrm{u}}}{2}} \mathrm{d}v + \pi\lambda_{\mathrm{g}} P_{\mathrm{g}}^n \int_{R_{\mathrm{s}}^2}^{\infty} \zeta\left(\sin^{-1}\frac{h_{\mathrm{u}}}{\sqrt{v}}\right) \\
&\quad \times \left\{\frac{(m+n-1)!}{m^n(m-1)!} v^{-\frac{n\alpha_{\mathrm{u}}}{2}} - n! v^{-\frac{n\alpha_{\mathrm{u}}}{2}}\right\} \mathrm{d}v \\
&= 2n!\pi\lambda_{\mathrm{g}} P_{\mathrm{g}}^n \frac{R_{\mathrm{s}}^{2-n\alpha_{\mathrm{u}}}}{n\alpha_{\mathrm{u}}-2} + \pi\lambda_{\mathrm{g}} P_{\mathrm{g}}^n \int_{R_{\mathrm{s}}^2}^{\infty} \zeta\left(\sin^{-1}\frac{h_{\mathrm{u}}}{\sqrt{v}}\right) \\
&\quad \times \left\{\frac{(m+n-1)!}{m^n(m-1)!} v^{-\frac{n\alpha_{\mathrm{u}}}{2}} - n! v^{-\frac{n\alpha_{\mathrm{u}}}{2}}\right\} \mathrm{d}v. \qquad (44)
\end{aligned}$$

Using the first and second cumulants of the random variable Z_0, the parameters μ_{Z_0} and $\sigma_{Z_0}^2$ of its log-normal approximation can be obtained as

$$\mu_{Z_0} = \ln \frac{\kappa_{Z_0,1}}{\sqrt{\frac{\kappa_{Z_0,2}}{\kappa_{Z_0,1}^2}+1}} \quad \text{and} \quad \sigma_{Z_0}^2 = \ln\left(\frac{\kappa_{Z_0,2}}{\kappa_{Z_0,1}^2}+1\right).$$

Similarly, using the first and second cumulants of the random variable Z, we can obtain μ_Z and σ_Z^2 as

$$\mu_{Z} = \ln \frac{\kappa_{Z,1}}{\sqrt{\frac{\kappa_{Z,2}}{\kappa_{Z,1}^2}+1}} \quad \text{and} \quad \sigma_{Z}^2 = \ln\left(\frac{\kappa_{Z,2}}{\kappa_{Z,1}^2}+1\right),$$

where

$$\begin{aligned}
\kappa_{Z,n} =& 2n!\pi\lambda_{\mathrm{g}} P_{\mathrm{g}}^n \frac{R_{\mathrm{s}}^{2-n\alpha_{\mathrm{u}}}}{n\alpha_{\mathrm{u}}-2} + \pi\lambda_{\mathrm{g}} P_{\mathrm{g}}^n \int_{h_{\mathrm{u}}^2}^{\infty} \zeta\left(\sin^{-1}\frac{h_{\mathrm{u}}}{\sqrt{v}}\right) \\
&\times \left\{\frac{(m+n-1)!}{m^n(m-1)!} v^{-\frac{n\alpha_{\mathrm{u}}}{2}} - n! v^{-\frac{n\alpha_{\mathrm{u}}}{2}}\right\} \mathrm{d}v. \qquad (45)
\end{aligned}$$

To compare the error probabilities of the proposed spectrum sensing scheme with those of the schemes in [10]–[12], [24], we evaluate (38) and (39), approximating the PDFs of Z_0 and Z as

$$\ln(Z_0) \approx_d \mathcal{N}(\mu_{Z_0}, \sigma_{Z_0}^2), \quad \ln(Z) \approx_d \mathcal{N}(\mu_Z, \sigma_Z^2).$$

D. CHANNEL ACCESS PROBABILITY

The channel access probability depends entirely on the spatial distribution of the GBSs and the performance of spectrum sensing. With perfect sensing, the channel access probability is $\exp(-\pi\lambda_{\mathrm{g}}(R_{\mathrm{s}}^2 - h_{\mathrm{u}}^2))$. In practice, sensing errors–false alarms and missed detections–modify this probability. This probability captures the effect of sensing errors on the spatial distribution of active UAVs in the secondary network. Due to the presence of these two types of errors, the density function of the active UAV distribution becomes more complex. The channel access probability in the case of UAV deployment with a fixed probability of false alarm is presented in the following lemma.

Lemma 2. *The channel access probability for each UAV during the spectrum sensing process over the GBS network, conditioned on a fixed probability of false alarm p_{f}^*, sensing range R_{s}, and UAV altitude h_{u}, is given by*

$$\gamma = \mathcal{L}^{-1}\left[\frac{1}{s}\exp\left(-\pi\lambda_{\mathrm{g}}\phi(s, h_{\mathrm{u}}^2)\right)\right](\tau)\Big|_{\tau=\frac{\beta^*-\sigma_{\mathrm{n}}^2}{P_{\mathrm{g}}}}. \qquad (46)$$

Proof:
Using the law of total probability, the channel access probability can be expressed as

$$\gamma = \mathbb{P}(\Psi_{\mathrm{g}}(\mathcal{D})=0)(1-p_{\mathrm{f}}^*) + \mathbb{P}(\Psi_{\mathrm{g}}(\mathcal{D})\neq 0)p_{\mathrm{m}}. \qquad (47)$$

Substituting p_{m} from Theorem 2, the void probability of the homogeneous PPP, and simplifying the resulting expression completes the proof of Lemma 2. ■

E. NETWORK-LEVEL ANALYSIS

1) ACTIVE UAV NETWORK MODELING WITH PPP-BASED APPROXIMATION AND LIMITATIONS

Since the secondary network consists of UAVs that access the spectrum via sensing, the resulting point process $\widetilde{\Psi}_{\mathrm{u}}$, representing the ground projections of active UAVs, is a Cox process [31] whose random intensity measure is governed by the random disks of radius $\sqrt{R_{\mathrm{s}}^2 - h_{\mathrm{u}}^2}$ and the missed detection probability p_{m}.

Consequently, an exact characterization of the Laplace transform of the aggregate interference-plus-noise experienced by users in both networks (denoted by I_{u} and $\hat{I}_{\mathrm{u}}$) is analytically intractable.

To enable tractable analysis, we approximate $\widetilde{\Psi}_{\mathrm{u}}$ as a homogeneous PPP obtained via independent thinning of the original UAV point process, where each UAV accesses the channel with probability γ. Accordingly, the density of the approximating PPP is given by $\gamma\lambda_{\mathrm{u}}$. This independent thinning assumption neglects the clustering of active UAVs induced by sensing and therefore results in performance results that upper bound the true performance.

In particular, as the density λ_{u} increases, the deviation of $\widetilde{\Psi}_{\mathrm{u}}$ from a PPP becomes more pronounced due to stronger sensing-induced correlations among UAVs. As a result, the PPP-based approximation becomes less accurate when $\lambda_{\rm u}/\lambda_{\rm g}$ is large. In contrast, when $\lambda_{\rm u}/\lambda_{\rm g} \approx 1$, the analytical results provide a tight approximation. This behavior is illustrated in Fig. 7, where the deviation between analytical and simulation results increases with the UAV density.

2) INTERFERENCE MODELING

The following lemma provides the Laplace transform of the interference-plus-noise for both networks.

Lemma 3. *The Laplace transform of the total interference-plus-noise experienced by the typical UAV user, conditioned on the random variable $r_{\rm u}^2$, is given by*

$$\mathcal{L}_{\widetilde{\Upsilon}|r_{\rm u}^2}(s) = \exp\left(-s\sigma_{\rm n}^2 - \frac{\pi\lambda_{\rm g}(sP_{\rm g})^{2/\alpha_{\rm g}}}{\operatorname{sinc}(2/\alpha_{\rm g})} - \pi\gamma\lambda_{\rm u}\mathcal{U}\left(sP_{\rm u}, r_{\rm u}^2 + h_{\rm u}^2\right)\right), \tag{48}$$

where $\mathcal{U}(a,b)$ for $a,b \in \mathbb{R}_+$ is defined as

$$\mathcal{U}(a,b) = \int_b^{\infty}\left[\frac{a}{a+v^{\frac{\alpha_{\rm u}}{2}}} - \zeta\left(\sin^{-1}\frac{h_{\rm u}}{\sqrt{v}}\right)\times \left\{\left(1+\frac{a}{mv^{\frac{\alpha_{\rm u}}{2}}}\right)^{-m} - \frac{1}{1+av^{-\frac{\alpha_{\rm u}}{2}}}\right\}\right]{\rm d}v. \tag{49}$$

Similarly, the Laplace transform of the total interference-plus-noise to the typical user in the GBS network, conditioned on the random variable $r_{\rm g}^2$, is given by

$$\mathcal{L}_{\Upsilon|r_{\rm g}^2}(s) = \exp\left[-s\sigma_{\rm n}^2 - \pi\lambda_{\rm g}r_{\rm g}^2\mathcal{G}\left(\frac{sP_{\rm g}}{r_{\rm g}^{\alpha_{\rm g}}}, \frac{2}{\alpha_{\rm g}}\right) - \pi\gamma\lambda_{\rm u}\mathcal{U}\left(sP_{\rm u}, h_{\rm u}^2\right)\right], \tag{50}$$

where $\mathcal{G}(a,b)$ for $a,b \in \mathbb{R}_+$ is given by

$$\mathcal{G}(a,b) = \int_{a^{-b}}^{\infty}\frac{a^b}{1+v^{\frac{1}{b}}}{\rm d}v = a^b\left(\frac{1}{\operatorname{sinc}(b)} - \int_0^{a^{-b}}\frac{1}{1+v^{\frac{1}{b}}}{\rm d}v\right). \tag{51}$$

Proof:
See Appendix B. ■

Remark 1. *Lemma 3 is derived under the assumption that the active UAV locations form a homogeneous PPP. This result can be extended to a finite UAV network modeled as a finite homogeneous PPP within a circular region of radius $R_{\rm f}$ in the sky, where the number of UAVs follows a Poisson distribution. In this case, $\mathcal{U}(a,b)$ in the lemma becomes*

$$\mathcal{U}_{\rm f}(a,b) = \int_b^{R_{\rm f}^2+h_{\rm u}^2}\left[\frac{a}{a+v^{\frac{\alpha_{\rm u}}{2}}} - \zeta\left(\sin^{-1}\frac{h_{\rm u}}{\sqrt{v}}\right) \times\left\{\left(1+\frac{a}{mv^{\frac{\alpha_{\rm u}}{2}}}\right)^{-m} - \frac{1}{1+av^{-\frac{\alpha_{\rm u}}{2}}}\right\}\right]{\rm d}v. \tag{52}$$

Remark 2. *We assume that all GBSs transmit on the considered frequency band, which corresponds to a fully loaded network, resulting in a worst-case interference scenario. In practice, dynamic scheduling reduces the set of active transmitters. This effect can be modeled by introducing an activity factor $p_{\rm tx} \in [0,1]$, which represents the probability that a GBS transmits on the target frequency. The resulting active GBSs form an independently thinned point process with effective density $p_{\rm tx}\lambda_{\rm g}$. This extension preserves analytical tractability, as all derived expressions can be directly adapted by replacing $\lambda_{\rm g}$ with $p_{\rm tx}\lambda_{\rm g}$, thus allowing the framework to account for both fully and partially loaded networks.*

3) SUCCESS PROBABILITY ANALYSIS

The downlink success probabilities of the typical GBS user and the typical UAV user are defined, respectively, as

$$p_{\rm c,g}(\eta) \triangleq \mathbb{P}[\Xi_{{\rm g},o} \geq \eta] \text{ and } p_{\rm c,u}(\eta) \triangleq \mathbb{P}[\Xi_{{\rm u},z} \geq \eta],$$

where $\eta > 0$ is the SINR threshold for successful decoding. In this work, we adopt a channel model that distinguishes between LoS and NLoS conditions. The channel power gain is modeled as the gamma distribution for LoS channels and as an exponential distribution for NLoS channels. A similar gamma-distributed channel power gain model, $\operatorname{Gamma}(N_{\rm u}, N_{\rm u})$, has been employed in multiple-input single-output (MISO) downlink systems, as reported in [32], where $N_{\rm u}$ denotes the number of antennas. Without loss of generality, we place the typical UAV user at $z = o$ and derive the success probability as follows:

$$p_{\rm c,u}(\eta) = \mathcal{L}^{-1}\left\{\frac{1}{s}\mathcal{L}_{\Xi_{{\rm u},o}^{-1}}(s)\right\}\left(\frac{1}{\eta}\right) = \mathcal{L}^{-1}\left\{\frac{1}{s}\mathbb{E}\left[\exp\left(-\frac{s\widetilde{\Upsilon}\left(r_{\rm u}^2+h_{\rm u}^2\right)^{\frac{\alpha_{\rm u}}{2}}}{P_{\rm u}\widetilde{\Omega}_{\rm u}}\right)\right]\right\}\left(\frac{1}{\eta}\right), \tag{55}$$

where the distance between the typical UAV user and the ground projection of the serving UAV follows a Rayleigh distribution [31], i.e., $r_{\rm u} \sim \operatorname{Rayleigh}\left(\frac{1}{\sqrt{2\pi\gamma\lambda_{\rm u}}}\right)$. The expectation in the above expression can be simplified as

$$\mathbb{E}\left[\exp\left(-\frac{s\widetilde{\Upsilon}(r_{\rm u}^2+h_{\rm u}^2)^{\frac{\alpha_{\rm u}}{2}}}{P_{\rm u}\widetilde{\Omega}_{\rm u}}\right)\right] = \mathbb{E}\left[\zeta\left(\tan^{-1}\frac{h_{\rm u}}{\sqrt{r_{\rm u}^2}}\right)\mathcal{L}_{\widetilde{\Upsilon}|r_{\rm u}^2}\left(\frac{s(r_{\rm u}^2+h_{\rm u}^2)^{\frac{\alpha_{\rm u}}{2}}}{P_{\rm u}\Omega_{\rm u}^{\rm L}}\right) + \left[1-\zeta\left(\tan^{-1}\frac{h_{\rm u}}{\sqrt{r_{\rm u}^2}}\right)\right]\mathcal{L}_{\widetilde{\Upsilon}|r_{\rm u}^2}\left(\frac{s(r_{\rm u}^2+h_{\rm u}^2)^{\frac{\alpha_{\rm u}}{2}}}{P_{\rm u}\Omega_{\rm u}^{\rm N}}\right)\right], \tag{56}$$

which comprises two components: one for LoS and the other for NLoS.

The expectation with respect to the LoS component is evaluated as follows:

$$\mathbb{E}_{\Omega_{\rm u}^{\rm L}}\left[\mathcal{L}_{\widetilde{\Upsilon}|r_{\rm u}^2}\left(\frac{s(r_{\rm u}^2+h_{\rm u}^2)^{\frac{\alpha_{\rm u}}{2}}}{P_{\rm u}\Omega_{\rm u}^{\rm L}}\right)\right]$$

$$
\begin{aligned}
p_{\mathrm{c,u}}(\eta) &= \mathbb{E}_{r_{\mathrm{u}}^2}\left[\frac{1}{(m-1)!}\zeta\left(\tan^{-1}\frac{h_{\mathrm{u}}}{\sqrt{r_{\mathrm{u}}^2}}\right)\left\{\frac{\mathrm{d}^{m-1}}{\mathrm{d}v^{m-1}}v^{m-1}\mathcal{L}_{\widetilde{\Upsilon}|r_{\mathrm{u}}^2}\left(\frac{m(r_{\mathrm{u}}^2+h_{\mathrm{u}}^2)^{\frac{\alpha_{\mathrm{u}}}{2}}}{P_{\mathrm{u}}v}\right)\right\} + \left(1-\zeta\left(\tan^{-1}\frac{h_{\mathrm{u}}}{\sqrt{r_{\mathrm{u}}^2}}\right)\right)\right.\\
&\quad \left.\left.\times\mathcal{L}_{\widetilde{\Upsilon}|r_{\mathrm{u}}^2}\left(\frac{\eta}{P_{\mathrm{u}}}(r_{\mathrm{u}}^2+h_{\mathrm{u}}^2)^{\frac{\alpha_{\mathrm{u}}}{2}}\right)\right]\right|_{v=\frac{1}{\eta}}\\
&\overset{(a)}{=} \mathbb{E}_{r_{\mathrm{u}}^2}\left\{\frac{1}{(m-1)!}\zeta\left(\tan^{-1}\frac{h_{\mathrm{u}}}{\sqrt{r_{\mathrm{u}}^2}}\right)\frac{\mathrm{d}^{m-1}}{\mathrm{d}v^{m-1}}v^{m-1}\exp\left[-\frac{m(r_{\mathrm{u}}^2+h_{\mathrm{u}}^2)^{\frac{\alpha_{\mathrm{u}}}{2}}\sigma_{\mathrm{n}}^2}{P_{\mathrm{u}}v} - \frac{\pi\lambda_{\mathrm{g}}(r_{\mathrm{u}}^2+h_{\mathrm{u}}^2)^{\frac{\alpha_{\mathrm{u}}}{\alpha_{\mathrm{g}}}}}{\mathrm{sinc}\left(\frac{2}{\alpha_{\mathrm{g}}}\right)}\left(\frac{mP_{\mathrm{g}}}{P_{\mathrm{u}}v}\right)^{\frac{2}{\alpha_{\mathrm{g}}}}\right.\right.\\
&\quad \left.-\pi\gamma\lambda_{\mathrm{u}}\mathcal{U}\left(\frac{m}{v}(r_{\mathrm{u}}^2+h_{\mathrm{u}}^2)^{\frac{\alpha_{\mathrm{u}}}{2}}, r_{\mathrm{u}}^2+h_{\mathrm{u}}^2\right)\right] + \left(1-\zeta\left(\tan^{-1}\frac{h_{\mathrm{u}}}{\sqrt{r_{\mathrm{u}}^2}}\right)\right)\exp\left(-\frac{\eta(r_{\mathrm{u}}^2+h_{\mathrm{u}}^2)^{\frac{\alpha_{\mathrm{u}}}{2}}\sigma_{\mathrm{n}}^2}{P_{\mathrm{u}}}\right.\\
&\quad \left.\left.\left.-\pi\lambda_{\mathrm{g}}\left(\frac{\eta P_{\mathrm{g}}}{P_{\mathrm{u}}}\right)^{\frac{2}{\alpha_{\mathrm{g}}}}\frac{(r_{\mathrm{u}}^2+h_{\mathrm{u}}^2)^{\frac{\alpha_{\mathrm{u}}}{\alpha_{\mathrm{g}}}}}{\mathrm{sinc}\left(\frac{2}{\alpha_{\mathrm{g}}}\right)} - \pi\gamma\lambda_{\mathrm{u}}\mathcal{U}\left(\eta(r_{\mathrm{u}}^2+h_{\mathrm{u}}^2)^{\frac{\alpha_{\mathrm{u}}}{2}}, r_{\mathrm{u}}^2+h_{\mathrm{u}}^2\right)\right)\right\}\right|_{v=\frac{1}{\eta}}. \qquad (53)
\end{aligned}
$$

$$
\begin{aligned}
p_{\mathrm{c,u}}(\eta) &\leq \mathbb{E}_{r_{\mathrm{u}}^2}\left\{\frac{1}{(m-1)!}\zeta\left(\tan^{-1}\frac{h_{\mathrm{u}}}{\sqrt{r_{\mathrm{u}}^2}}\right)\frac{\mathrm{d}^{m-1}}{\mathrm{d}v^{m-1}}v^{m-1}\exp\left[-\frac{m(r_{\mathrm{u}}^2+h_{\mathrm{u}}^2)^{\frac{\alpha_{\mathrm{u}}}{2}}\sigma_{\mathrm{n}}^2}{P_{\mathrm{u}}v} - \pi\lambda_{\mathrm{g}}R_{\mathrm{d}}^2\mathcal{G}\left(\frac{mP_{\mathrm{g}}}{vP_{\mathrm{u}}}\frac{(r_{\mathrm{u}}^2+h_{\mathrm{u}}^2)^{\frac{\alpha_{\mathrm{u}}}{2}}}{R_{\mathrm{d}}^{\alpha_{\mathrm{g}}}}, \frac{2}{\alpha_{\mathrm{g}}}\right)\right.\right.\\
&\quad \left.-\pi\gamma\lambda_{\mathrm{u}}\mathcal{U}\left(\frac{m}{v}(r_{\mathrm{u}}^2+h_{\mathrm{u}}^2)^{\frac{\alpha_{\mathrm{u}}}{2}}, r_{\mathrm{u}}^2+h_{\mathrm{u}}^2\right)\right] + \left(1-\zeta\left(\tan^{-1}\frac{h_{\mathrm{u}}}{\sqrt{r_{\mathrm{u}}^2}}\right)\right)\exp\left(-\frac{\eta(r_{\mathrm{u}}^2+h_{\mathrm{u}}^2)^{\frac{\alpha_{\mathrm{u}}}{2}}\sigma_{\mathrm{n}}^2}{P_{\mathrm{u}}}\right.\\
&\quad \left.\left.\left.-\pi\lambda_{\mathrm{g}}R_{\mathrm{d}}^2\mathcal{G}\left(\frac{\eta P_{\mathrm{g}}}{P_{\mathrm{u}}}\frac{(r_{\mathrm{u}}^2+h_{\mathrm{u}}^2)^{\frac{\alpha_{\mathrm{u}}}{2}}}{R_{\mathrm{d}}^{\alpha_{\mathrm{g}}}}, \frac{2}{\alpha_{\mathrm{g}}}\right) - \pi\gamma\lambda_{\mathrm{u}}\mathcal{U}\left(\eta(r_{\mathrm{u}}^2+h_{\mathrm{u}}^2)^{\frac{\alpha_{\mathrm{u}}}{2}}, r_{\mathrm{u}}^2+h_{\mathrm{u}}^2\right)\right)\right\}\right|_{v=\frac{1}{\eta}}. \qquad (54)
\end{aligned}
$$

$$
\begin{aligned}
&= \int_0^\infty \mathcal{L}_{\widetilde{\Upsilon}|r_{\mathrm{u}}^2}\left(\frac{s(r_{\mathrm{u}}^2+h_{\mathrm{u}}^2)^{\frac{\alpha_{\mathrm{u}}}{2}}}{P_{\mathrm{u}}\omega_l}\right)f_{\Omega_{\mathrm{u}}^{\mathrm{L}}}(\omega_l)\mathrm{d}\omega_l\\
&\overset{(a)}{=} s\frac{1}{m}\int_0^\infty \mathcal{L}_{\widetilde{\Upsilon}|r_{\mathrm{u}}^2}\left(\frac{m(r_{\mathrm{u}}^2+h_{\mathrm{u}}^2)^{\frac{\alpha_{\mathrm{u}}}{2}}}{P_{\mathrm{u}}v}\right)f_{\Omega_{\mathrm{u}}^{\mathrm{L}}}\left(\frac{sv}{m}\right)\mathrm{d}v\\
&= \frac{s}{(m-1)!}\left[s^{m-1}\int_0^\infty v^{m-1}\mathcal{L}_{\widetilde{\Upsilon}|r_{\mathrm{u}}^2}\left(\frac{m(r_{\mathrm{u}}^2+h_{\mathrm{u}}^2)^{\frac{\alpha_{\mathrm{u}}}{2}}}{P_{\mathrm{u}}v}\right)\times\right.\\
&\qquad \left. e^{-sv}\mathrm{d}v\right]\\
&= \frac{s}{(m-1)!}\mathcal{L}\left\{\frac{\mathrm{d}^{m-1}}{\mathrm{d}v^{m-1}}v^{m-1}\times\right.\\
&\qquad \left.\mathcal{L}_{\widetilde{\Upsilon}|r_{\mathrm{u}}^2}\left(\frac{m(r_{\mathrm{u}}^2+h_{\mathrm{u}}^2)^{\frac{\alpha_{\mathrm{u}}}{2}}}{P_{\mathrm{u}}v}\right)\right\}(s), \qquad (57)
\end{aligned}
$$

where (a) follows from a change of variables.

Likewise, the expectation of the second term in (56) can be derived as

$$
\begin{aligned}
&\mathbb{E}_{\Omega_{\mathrm{u}}^{\mathrm{N}}}\left[\mathcal{L}_{\widetilde{\Upsilon}|r_{\mathrm{u}}^2}\left(\frac{s(r_{\mathrm{u}}^2+h_{\mathrm{u}}^2)^{\frac{\alpha_{\mathrm{u}}}{2}}}{P_{\mathrm{u}}\Omega_{\mathrm{u}}^{\mathrm{N}}}\right)\right]\\
&\qquad = s\mathcal{L}\left\{\mathcal{L}_{\widetilde{\Upsilon}|r_{\mathrm{u}}^2}\left(\frac{(r_{\mathrm{u}}^2+h_{\mathrm{u}}^2)^{\frac{\alpha_{\mathrm{u}}}{2}}}{P_{\mathrm{u}}v}\right)\right\}(s). \qquad (59)
\end{aligned}
$$

The final expression for the success probability of the typical UAV user is then given in (53), where step (a) follows from Lemma 3 and $r_{\mathrm{u}}^2 \sim \mathrm{Exp}(\pi\gamma\lambda_{\mathrm{u}})$.

Similarly, the success probability of the typical GBS user located at the origin, $p_{\mathrm{c,g}}(\eta) = \mathbb{P}[\Xi_{\mathrm{g},o} \geq \eta]$, is

$$
\mathbb{P}\left[\frac{P_{\mathrm{g}}r_{\mathrm{g}}^{-\alpha_{\mathrm{g}}}\Omega_{\mathrm{g},o}}{\Upsilon} \geq \eta\right] = \mathbb{E}_{r_{\mathrm{g}}}\left[\mathcal{L}_{\Upsilon|r_{\mathrm{g}}}\left(\frac{\eta r_{\mathrm{g}}^{\alpha_{\mathrm{g}}}}{P_{\mathrm{g}}}\right)\right],
$$

where $r_{\mathrm{g}} \sim \mathrm{Rayleigh}\left(\frac{1}{\sqrt{2\pi\lambda_{\mathrm{g}}}}\right)$. Using Lemma 3, we obtain:

$$
\begin{aligned}
p_{\mathrm{c,g}}(\eta) =& \mathbb{E}_{r_{\mathrm{g}}^2}\left[\exp\left(-\frac{\sigma_{\mathrm{n}}^2\eta r_{\mathrm{g}}^{\alpha_{\mathrm{g}}}}{P_{\mathrm{g}}} - \pi\lambda_{\mathrm{g}}r_{\mathrm{g}}^2\mathcal{G}\left(\eta, \frac{2}{\alpha_{\mathrm{g}}}\right)\right.\right.\\
&\left.\left.-\pi\gamma\lambda_{\mathrm{u}}\mathcal{U}\left(\frac{\eta P_{\mathrm{u}}r_{\mathrm{g}}^{\alpha_{\mathrm{g}}}}{P_{\mathrm{g}}}, h_{\mathrm{u}}^2\right)\right)\right], \qquad (60)
\end{aligned}
$$

where $r_{\mathrm{g}}^2 \sim \mathrm{Exp}\,(\pi\lambda_{\mathrm{g}})$.

Since the success probability of the UAV user given in (53) is derived by approximating the network as a homogeneous PPP via independent thinning, the corresponding upper bound can be obtained by conditioning on the absence of GBSs within a distance of $R_{\mathrm{d}} = \sqrt{R_{\mathrm{s}}^2 - h_{\mathrm{u}}^2}$ centered at the location of the typical user. Based on this condition, the Laplace transform $\mathcal{L}_{\widetilde{\Upsilon}|r_{\mathrm{u}}^2}(s)$ given in Lemma 3 can be rewritten as

$$
\mathcal{L}_{\widetilde{\Upsilon}|r_{\mathrm{u}}^2}(s) = e^{-s\sigma_{\mathrm{n}}^2 - \pi\lambda_{\mathrm{g}}R_{\mathrm{d}}^2\mathcal{G}\left(sP_{\mathrm{g}}R_{\mathrm{d}}^{-\alpha_{\mathrm{g}}}, \frac{2}{\alpha_{\mathrm{g}}}\right) - \pi\gamma\lambda_{\mathrm{u}}\mathcal{U}\left(sP_{\mathrm{u}}, r_{\mathrm{u}}^2+h_{\mathrm{u}}^2\right)}. \qquad (61)
$$

Substituting the above Laplace transform into (57) and (59), the upper bound of $p_{\mathrm{c,u}}(\eta)$ can be expressed as in (54).

$$\begin{aligned}\mathcal{C}_{\mathrm{u}} =&\mathbb{E}\left[\zeta\left(\tan^{-1}\frac{h_{\mathrm{u}}}{\sqrt{r_{\mathrm{u}}^2}}\right)\log_2\left(1+\frac{P_{\mathrm{u}}(r_{\mathrm{u}}^2+h_{\mathrm{u}}^2)^{\frac{\alpha_{\mathrm{u}}}{2}}\Omega_{\mathrm{u}}^{L}}{\widetilde{\Upsilon}}\right)+\left[1-\zeta\left(\tan^{-1}\frac{h_{\mathrm{u}}}{\sqrt{r_{\mathrm{u}}^2}}\right)\right]\log_2\left(1+\frac{P_{\mathrm{u}}(r_{\mathrm{u}}^2+h_{\mathrm{u}}^2)^{\frac{\alpha_{\mathrm{u}}}{2}}\Omega_{\mathrm{u}}^{N}}{\widetilde{\Upsilon}}\right)\right]\\
=&\frac{1}{\ln(2)}\int_{0^+}^{\infty}\frac{1}{z}\mathbb{E}_{r_{\mathrm{u}}^2}\left[\zeta\left(\tan^{-1}\frac{h_{\mathrm{u}}}{\sqrt{r_{\mathrm{u}}^2}}\right)\left\{1-\mathcal{L}_{\Omega_{\mathrm{u}}^{\mathrm{L}}}(z)\right\}\mathcal{L}_{\widetilde{\Upsilon}|r_{\mathrm{u}}^2}\left(\frac{z(r_{\mathrm{u}}^2+h_{\mathrm{u}}^2)^{\frac{\alpha_{\mathrm{u}}}{2}}}{P_{\mathrm{u}}}\right)+\left\{1-\zeta\left(\tan^{-1}\frac{h_{\mathrm{u}}}{\sqrt{r_{\mathrm{u}}^2}}\right)\right\}\left\{1-\mathcal{L}_{\Omega_{\mathrm{u}}^{\mathrm{N}}}(z)\right\}\right.\\
&\left.\times\,\mathcal{L}_{\widetilde{\Upsilon}|r_{\mathrm{u}}^2}\left(\frac{z(r_{\mathrm{u}}^2+h_{\mathrm{u}}^2)^{\frac{\alpha_{\mathrm{u}}}{2}}}{P_{\mathrm{u}}}\right)\right]\\
=&\frac{1}{\ln(2)}\int_{0^+}^{\infty}\frac{1}{z}\mathbb{E}_{r_{\mathrm{u}}^2}\left[\left\{\zeta\left(\tan^{-1}\frac{h_{\mathrm{u}}}{\sqrt{r_{\mathrm{u}}^2}}\right)\left(1-\left(\frac{m}{m+z}\right)^{m}\right)+\left(1-\zeta\left(\tan^{-1}\frac{h_{\mathrm{u}}}{\sqrt{r_{\mathrm{u}}^2}}\right)\right)\frac{z}{1+z}\right\}\right.\\
&\left.\times\exp\left(-\frac{s(r_{\mathrm{u}}^2+h_{\mathrm{u}}^2)^{\frac{\alpha_{\mathrm{u}}}{2}}\sigma_{\mathrm{n}}^2}{P_{\mathrm{u}}}-\pi\lambda_{\mathrm{g}}\left(\frac{sP_{\mathrm{g}}}{P_{\mathrm{u}}}\right)^{\frac{2}{\alpha_{\mathrm{g}}}}\frac{(r_{\mathrm{u}}^2+h_{\mathrm{u}}^2)^{\frac{\alpha_{\mathrm{u}}}{\alpha_{\mathrm{g}}}}}{\mathrm{sinc}\left(\frac{2}{\alpha_{\mathrm{g}}}\right)}-\pi\gamma\lambda_{\mathrm{u}}\mathcal{U}\left(s(r_{\mathrm{u}}^2+h_{\mathrm{u}}^2)^{\frac{\alpha_{\mathrm{u}}}{2}},r_{\mathrm{u}}^2+h_{\mathrm{u}}^2\right)\right)\right]\mathrm{d}z.\end{aligned} \tag{58}$$

Remark 3. *The success probabilities of the typical users in both the UAV network and the GBS network are derived assuming a common UAV altitude. In practice, UAVs may hover within a range of altitudes due to flight-control disturbances or weather conditions such as wind. For example, if the UAV altitude h_{u} follows a uniform distribution, i.e., $h_{\mathrm{u}} \sim U(a,b)$, the success probabilities of the typical UAV user and GBS user can be derived using* (53) *and* (60) *as* $\frac{1}{b-a}\int_a^b p_{\mathrm{c,u}}(\eta,h)\mathrm{d}h$ *and* $\frac{1}{b-a}\int_a^b p_{\mathrm{c,g}}(\eta,h)\mathrm{d}h$*, respectively. In this case, the additional integration increases the computational complexity to $\mathcal{O}(L^3)$, where L denotes the number of function evaluations, which still permits an efficient evaluation.*

4) JOINT SUCCESS PROBABILITY STATISTICS

The joint success probability of the two typical users, $\mathbb{P}[\Xi_{\mathrm{g},o} \geq \eta, \Xi_{\mathrm{u},z} \geq \eta]$, is influenced by their relative positions and exhibits a negative correlation between the individual success probabilities. In the special case when the typical UAV user is located at the origin, $z = o$, if the typical GBS user experiences a high success probability due to its proximity to the serving GBS, the typical UAV user tends to have a low success probability because of its relatively larger distance from its serving UAV, resulting in a strong negative correlation. Since the two random variables $\Xi_{\mathrm{g},o}$ and $\Xi_{\mathrm{u},z}$ are negatively quadrant dependent with respect to z, their joint distribution satisfies the upper bound [33]

$$\mathbb{P}[\Xi_{\mathrm{g},o} \geq \eta, \Xi_{\mathrm{u},z} \geq \eta] \leq \mathbb{P}[\Xi_{\mathrm{g},o} \geq \eta]\mathbb{P}[\Xi_{\mathrm{u},z} \geq \eta]. \tag{62}$$

Equality holds only when $\|z\| \gg R_{\mathrm{d}}$, where the two success events become independent. The difference between the two sides of the inequality, $\mathbb{P}[\Xi_{\mathrm{g},o} \geq \eta, \Xi_{\mathrm{u},z} \geq \eta] - \mathbb{P}[\Xi_{\mathrm{g},o} \geq \eta]\mathbb{P}[\Xi_{\mathrm{u},z} \geq \eta]$, reaches its maximum when $\|z\| = 0$.

5) THROUGHPUT ANALYSIS

The mean achievable throughput (in bps/Hz) for the typical user in either network is defined using the Shannon–Hartley theorem as

$$\begin{aligned}\mathcal{C}_x \triangleq \mathbb{E}\left[\log_2\left(1+\Xi_{x,o}\right)\right] &\overset{(a)}{=} \int_0^{\infty}\mathbb{P}\left(\Xi_{x,o} > 2^v - 1\right)\mathrm{d}v\\
&= \int_0^{\infty} p_{c,x}(2^v-1)\mathrm{d}v,\end{aligned} \tag{63}$$

where (a) follows from the fact that for a non-negative random variable: $\mathbb{E}[Z] = \int_0^{\infty}\mathbb{P}(Z > z)\mathrm{d}z$, for $x \in \{g, u\}$.

Alternatively, the mean throughput of the UAV network can be expressed directly as

$$\mathcal{C}_{\mathrm{u}} = \mathbb{E}\left[\log_2\left(1+\frac{P_{\mathrm{u}}\left(r_{\mathrm{u}}^2+h_{\mathrm{u}}^2\right)^{-\frac{\alpha_{\mathrm{u}}}{2}}\widetilde{\Omega}_{\mathrm{u},o}}{\widetilde{\Upsilon}}\right)\right]. \tag{64}$$

To evaluate (64), we employ the Shannon transform identity [34]:

$$\begin{aligned}&\mathbb{E}\left[\log_2\left(1+\frac{X}{Y+a}\right)\right]\\
&\quad= \frac{1}{\ln 2}\int_{0^+}^{\infty}\frac{\mathcal{L}_Y(z)(1-\mathcal{L}_X(z))}{ze^{az}}\mathrm{d}z,\end{aligned} \tag{65}$$

where X and Y are independent non-negative random variables, and a is a constant. Using this and Lemma 3, the mean achievable throughput of the UAV network is derived in (58).

Similarly, the mean achievable throughput of the typical GBS user is

$$\begin{aligned}\mathcal{C}_{\mathrm{g}} = \frac{1}{\ln 2}\int_{0^+}^{\infty}\frac{1}{1+s}\mathbb{E}_{r_{\mathrm{g}}^2}\Bigg\{\exp\Bigg(-\frac{sr_{\mathrm{g}}^{\alpha_{\mathrm{g}}}\sigma_{\mathrm{n}}^2}{P_{\mathrm{g}}}-\\
\pi\lambda_{\mathrm{g}}r_{\mathrm{g}}^2\mathcal{G}\left(s,\frac{2}{\alpha_{\mathrm{g}}}\right)-\pi\gamma\lambda_{\mathrm{u}}\mathcal{U}\left(\frac{sP_{\mathrm{u}}r_{\mathrm{g}}^{\alpha_{\mathrm{g}}}}{P_{\mathrm{g}}},h_{\mathrm{u}}^2\right)\Bigg)\Bigg\}\mathrm{d}s.\end{aligned} \tag{66}$$

6) JOINT THROUGHPUT STATISTICS

Following Sec. III.E.4, the upper bound of the joint throughput of the networks can be expressed as

$$\begin{aligned}&\mathbb{E}\left[\left\{\log_2\left(1+\Xi_{\mathrm{g},o}\right)\right\}\left\{\log_2\left(1+\Xi_{\mathrm{u},z}\right)\right\}\right]\\
&\leq \mathbb{E}\left[\log_2\left(1+\Xi_{\mathrm{g},o}\right)\right]\mathbb{E}\left[\log_2\left(1+\Xi_{\mathrm{u},z}\right)\right].\end{aligned} \tag{67}$$

TABLE 2. Network Parameters for Simulation [27], [32]

Parameter	GBS	UAV
Transmit power (W) $P_{\rm g}, P_{\rm u}$	30	1.5
density (BSs/m^2) $\lambda_{\rm g}, \lambda_{\rm u}$	1×10^{-5}	1×10^{-5}
Nakagami - m parameter for LoS	4	
Number of signal samples $N_{\rm s}$ (for sensing)	1000	
Spectrum sensing range $R_{\rm s}$ (m)	$150 \sim 300$	
Maximum altitude $h_{\rm u}$ (m)	N/A	$h_{\rm u} < 140$
Distance between the typical users z (m)	$0 \sim 500$	
Path-loss exponent $\alpha_{\rm g}, \alpha_{\rm u}$	3.5	2.8
Parameters (c_1, c_2) in (1) for suburban	$(24.5811, 39.5971)$	
Probability of false alarm $p_{\rm f}^*$	0.1	
Noise power (dBm) $\sigma_{\rm n}^2$	-110	

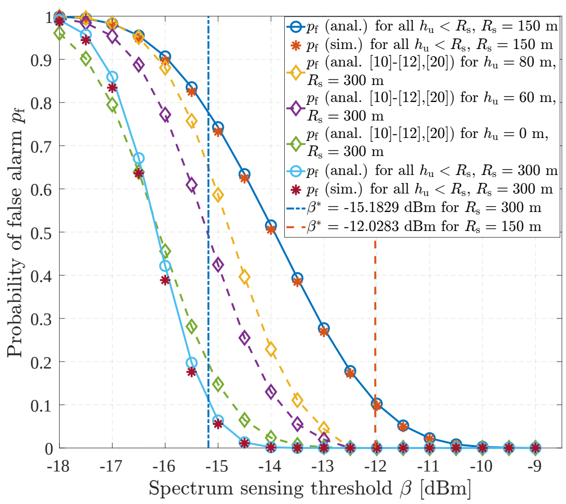

FIGURE 2. **Probability of false alarm.**

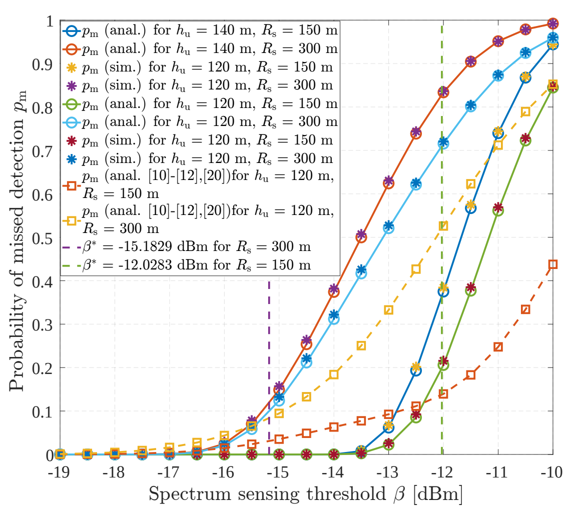

FIGURE 3. **Probability of missed detection.**

IV. NUMERICAL RESULTS

In this section, we present numerical results to validate the analytical findings. We first illustrate the performance of the proposed spectrum sensing scheme in terms of error probabilities, and then evaluate the network performance in terms of success probability and achievable throughput.

All results are obtained via Monte Carlo simulations of a large-scale network comprising GBSs and UAVs in a suburban environment. The network parameters are listed in Table 2 and are chosen based on real statistical data analyzed in [27] and [32].

A. Simulation Results of the Spectrum Sensing Errors

The variation of the probability of false alarm $p_{\rm f}$ with respect to the detection threshold β is shown in Fig. 2 for two sensing radii, $R_{\rm s} = 150$ m and $R_{\rm s} = 300$ m. As stated in Theorem 2, $p_{\rm f}$ is independent of the UAV altitude $h_{\rm u}$, which is confirmed by both the analytical and simulation results for $R_{\rm s} = 150$ m and $R_{\rm s} = 300$ m. In contrast, the analytical results based on the scheme in [10]–[12], [24] indicate that $p_{\rm f}$ depends on $h_{\rm u}$. These results are presented for three different UAV altitudes–0 m, 60 m, and 80 m–with $R_{\rm s} = 300$ m. Among them, the case $h_{\rm u} = 0$ m matches most closely with the simulation results because, in this case, the probability of LoS is negligible and the NLoS channel is modeled as Rayleigh fading. At higher altitudes, the LoS probability increases and the channel follows Nakagami-m fading, which affects the results even when normalized channel power gain is used. Such limitations in prior schemes lead to deviations from the simulation results, whereas the proposed scheme overcomes these limitations.

Similar to Fig. 2, the analytical results of the probability of missed detection $p_{\rm m}$ in Fig. 3 show that the analytical results of the proposed scheme almost perfectly match the simulation results due to the exact mathematical expressions, whereas the results from the related works only partially follow the simulation trends–particularly for $h_{\rm u} = 120$ m at $R_{\rm s} = 150$ m and $R_{\rm s} = 300$ m, where the deviation is more pronounced. Notably, for fixed $h_{\rm u}$, increasing $R_{\rm s}$ increases $p_{\rm m}$, whereas $p_{\rm f}$ decreases. This behavior can be explained under the $\mathcal{H}_1$ hypothesis: a smaller $R_{\rm s}$ implies a denser presence of GBSs within the sensing range, which strengthens the received signal and reduces $p_{\rm m}$. Overall, the simulation results almost perfectly coincide with the corresponding analytical results provided in Theorem 2 due to the exact mathematical expressions.

B. SIMULATION RESULTS FOR NETWORK PERFORMANCE

Fig. 4 illustrates the success probabilities for $R_{\rm s} = 150$ m and $R_{\rm s} = 250$ m at $h_{\rm u} = 60$ m for both UAV and GBS networks. The simulation results deviate slightly from the analytical curves due to approximations in the analysis. Specifically, instead of using the exact distribution of the active UAVs, we approximate their distribution as a homogeneous PPP. As $R_{\rm s}$ increases, the likelihood of spectrum sharing decreases, reducing the density of UAVs accessing the spectrum. Consequently, the UAV success probability $p_{\rm c,u}$ decreases, while the GBS success probability $p_{\rm c,g}$ in-

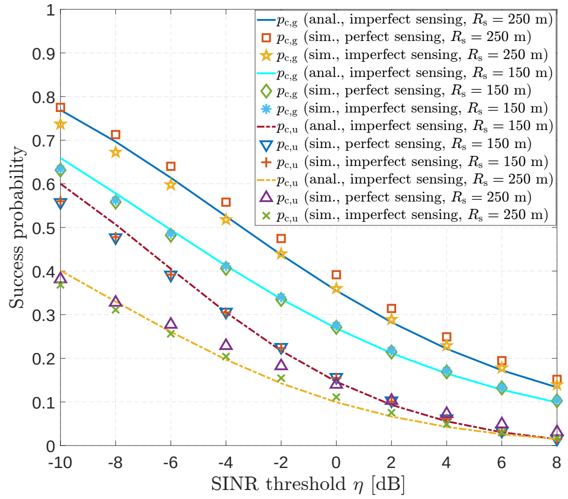

FIGURE 4. Probability of success, with a fixed probability of false alarm $p_f^* = 0.1$, and altitude $h_u = 60$ m.

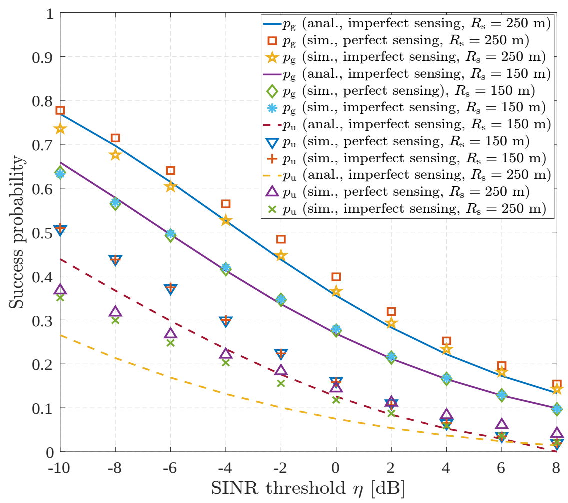

FIGURE 5. Probability of success, with a fixed probability of false alarm $p_f^* = 0.1$, and altitude $h_u = 60$ m in an urban environment.

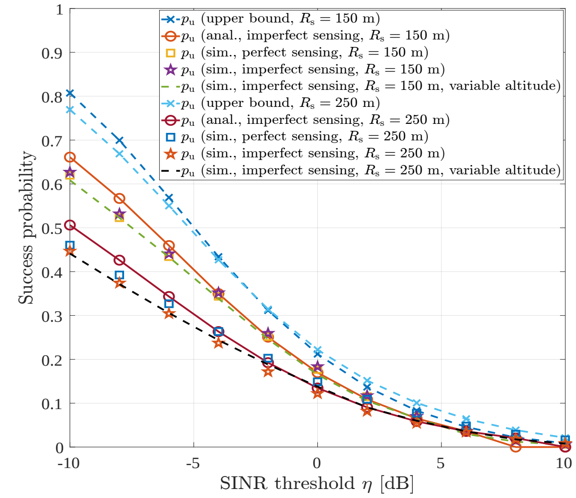

FIGURE 6. Probability of success, with a fixed probability of false alarm $p_f^* = 0.1$, dynamic scheduling of GBSs with $p_{tx} = 0.8$ (80 % of GBSs use the target spectrum), fixed altitude $h_u = 60$ m, and variable altitude $h \sim$ Uni$[h_u - 10, h_u + 10]$.

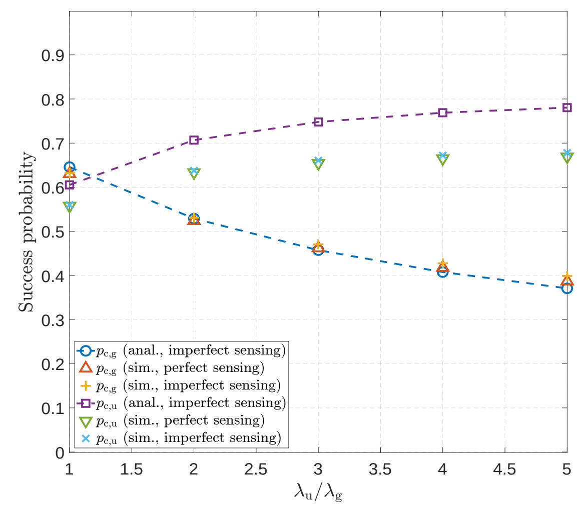

FIGURE 7. Probability of success, with a fixed probability of false alarm $p_f^* = 0.1$, GBS density $\lambda_g = 10^{-5}$ BSs/m^2, altitude $h_u = 60$ m, sensing range $R_s = 150$ m, R_s = 150 m, and SINR threshold η = -10 dB.

creases because of reduced UAV interference. Likewise, Fig. 5 depicts the success probabilities for the same parameters used in Fig. 4 and highlights the impact of propagation conditions in an urban environment. Clearly, the success probability of the GBS network remains unchanged, whereas the UAV network exhibits a noticeable deviation between suburban and urban propagation environments. For the urban environment, the parameters in (1) are set to $c_1 = 9.1$ and $c_2 = 43.91$.

Furthermore, this paper primarily focuses on a fully loaded GBS network, in which every GBS utilizes the target spectrum, representing a worst-case interference scenario. In practical cellular networks, however, GBSs may employ dynamic scheduling mechanisms, resulting in partially loaded networks. This is discussed in Remark 2. As shown in Fig. 6, the 80% loaded GBS network reduces the interference experienced by the UAV network, thereby increasing the success probability. The figure also presents the upper bound on the success probability, given in (54), as well as the success probability for the case where the UAV altitudes follow a uniform distribution, i.e., $h \sim \text{Uni}[h_u - 10, h_u + 10]$. The results indicate that such altitude variations have only a minor impact on network performance.

From Fig. 7, we observe how the success probability of both networks varies with λ_u/λ_g. While the analytical results for the GBS network closely match the simulation results, those for the UAV network exhibit deviations, due to the approximation of the UAV point process. This discrepancy increases with the ratio of the intensities. Specifically, the sensing-based deployed UAV network is modeled approximately as a homogeneous PPP, which provides nearly accurate predictions when the intensities of the UAV and GBS networks are comparable. Moreover, Fig. 8 illustrates the dependency between the joint success probability of the

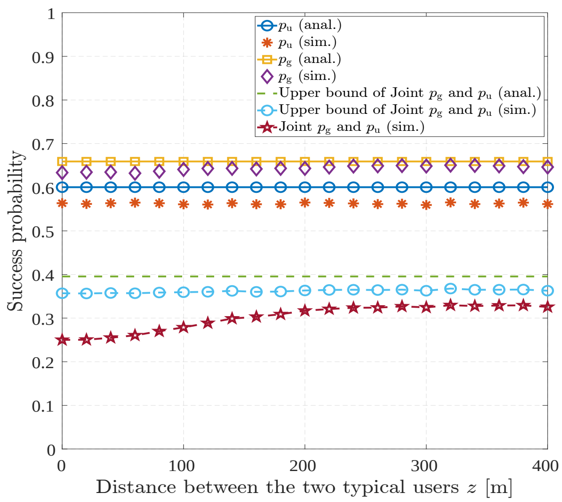

FIGURE 8. Joint success probability with altitude $h_{\mathrm{u}} = 60$ m, sensing range $R_{\mathrm{s}} = 150$ m, SINR threshold $\eta = -10$ dB, and a fixed probability of false alarm of $p_{\mathrm{f}}^{*} = 0.1$.

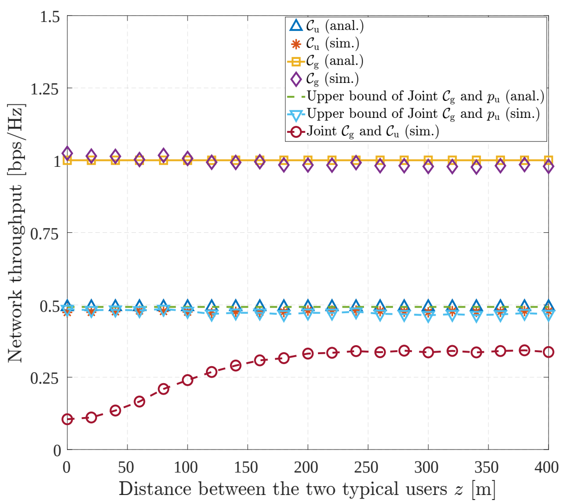

FIGURE 9. Joint throughput, with altitude $h_{\mathrm{u}} = 60$ m, sensing range $R_{\mathrm{s}} = 150$ m, and a fixed probability of false alarm of $p_{\mathrm{f}}^{*} = 0.1$.

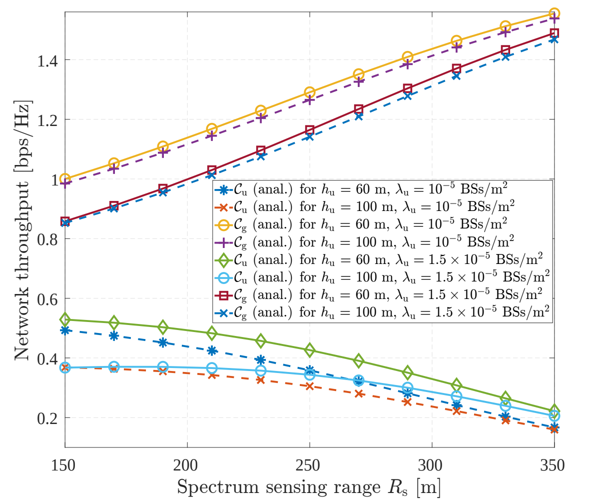

FIGURE 10. Throughput of GBS network and UAV network, with a fixed probability of false alarm $p_{\mathrm{f}}^{*} = 0.1$.

two typical users and their relative distance. The effect of negative association is most pronounced when the distance between the users is within the sensing range $R_{\mathrm{s}} = 150$ m, as shown in Fig. 8. As the relative distance increases, this dependency becomes less significant. Similarly, Fig. 9 presents the joint throughput of the two typical users, where a comparable trend in throughput variation is observed. However, a noticeable deviation between the upper bound and the simulation results appears when the relative distance between the typical users becomes large. In the joint throughput analysis, the nonlinear function $\log_2(1 + \Xi)$ distorts the relative spacing between the values of $\Xi_{\mathrm{g},o}$ and $\Xi_{\mathrm{u},z}$, which can make otherwise almost uncorrelated variables appear more correlated depending on their distribution.

Fig. 10 presents the throughputs of the UAV ($\mathcal{C}_{\mathrm{u}}$) and GBS ($\mathcal{C}_{\mathrm{g}}$) networks versus R_{s} for a fixed UAV altitude of $h_{\mathrm{u}} = 60$ m and two UAV network intensities, $\lambda_{\mathrm{u}} = 1 \times 10^{-5}$ BSs/m^2 and $\lambda_{\mathrm{u}} = 1.5 \times 10^{-5}$ BSs/m^2. These results follow the same trends as the success probabilities. A larger R_{s} reduces the interfering signal power from UAVs to the GBS network, which increases $\mathcal{C}_{\mathrm{g}}$ but decreases $\mathcal{C}_{\mathrm{u}}$. Likewise, as the UAV density increases, $\mathcal{C}_{\mathrm{u}}$ increases, while $\mathcal{C}_{\mathrm{g}}$ decreases.

V. CONCLUSIONS

This work presented a spectrum-sensing-based spectrum-sharing framework that enables a large-scale UAV network to opportunistically access the licensed spectrum of a GBS network. The proposed spectrum-sensing analysis is fundamentally different from existing approaches used in similar network settings, offering substantially improved tractability and accuracy. Its effectiveness stems from the availability of exact mathematical expressions, which significantly reduce computational complexity compared with prior methods.

The UAV altitude and sensing range play pivotal roles in determining both the sensing error probabilities and the overall network performance. For practical network deployment, the Neyman-Pearson detection framework bridges the gap between fixed sensing-error constraints and the throughput requirements of the network by jointly capturing the effects of UAV altitude and sensing range. Furthermore, characterizing the joint statistics of network performance metrics is critical, particularly when the relative distance between the typical users in the primary and secondary networks is smaller than the sensing range. In such scenarios, the joint success probability and the joint throughput exhibit negative quadrant dependence. This dependence disappears for the joint success probability when the relative distance becomes sufficiently larger than the sensing range, whereas the joint throughput retains a certain degree of dependence. Finally, since this work focused on the physical-layer characterization of spectrum access opportunities and adopted a PPP-based approximation, the clustering of UAVs induced by the spectrum access scheme remains a future direction of research to provide a more accurate network model.

APPENDIX

A. PROOF OF THEOREM 1

Since $\widetilde{T}_0$ is a non-negative random variable, its Laplace transform, $\mathcal{L}_{\widetilde{T}_0}(s) = \mathbb{E}\left[e^{-s\widetilde{T}_0}\right]$, is given by

$$\begin{aligned}\mathcal{L}_{\widetilde{T}_0}(s) &= \mathbb{E}\left[\exp\left\{-s\sum_{x\in\Psi_{\rm g}\setminus\Psi_{\rm g}(\mathcal{D})}\|(y_{\rm s},h_{\rm u})-(x,0)\|^{-\alpha_{\rm u}}\right\}\right]\\ &= \mathbb{E}\left[\prod_{x\in\Psi_{\rm g}\setminus\Psi_{\rm g}(\mathcal{D})}\exp\left(-s(\|y_s-x\|^2+h_{\rm u}^2)^{-\frac{\alpha_{\rm u}}{2}}\right)\right]\\ &\overset{(a)}{=} \mathbb{E}\left[\prod_{x\in\Psi'_{\rm g}\setminus\Psi'_{\rm g}(\mathcal{D})}\exp\left(-s\left(\|x'\|^2+h_{\rm u}^2\right)^{-\frac{\alpha_{\rm u}}{2}}\right)\right],\end{aligned} \tag{V.1}$$

where (a) follows from shifting the origin to $y_{\rm s}$. As shifting the origin preserves relative point locations, $\Psi'_{\rm g}$ remains a homogeneous PPP with density $\lambda_{\rm g}$. Applying the probability generating functional (PGFL) of the PPP [31] to $\Psi'_{\rm g}$ in step (a), we get:

$$\begin{aligned}&\exp\left[-2\pi\lambda_{\rm g}\int_{\sqrt{R_s^2-h_{\rm u}^2}}^{\infty}\left\{1-e^{\left(-s\left(r^2+h_{\rm u}^2\right)^{-\frac{\alpha_{\rm u}}{2}}\right)}\right\}r\mathrm{d}r\right]\\ &\overset{(b)}{=}\exp\left[-\pi\lambda_{\rm g}\int_{R_s^2-h_{\rm u}^2}^{\infty}\left\{1-\exp\left(-s\left(v+h_{\rm u}^2\right)^{-\frac{\alpha_{\rm u}}{2}}\right)\right\}\mathrm{d}v\right]\\ &\overset{(c)}{=}\exp\left[-\pi\lambda_{\rm g}\int_{R_s^2}^{\infty}\left\{1-\exp\left(-sp^{-\frac{\alpha_{\rm u}}{2}}\right)\right\}\mathrm{d}p\right],\end{aligned} \tag{V.2}$$

where (b) follows from the change of variable $r^2\to v$ and (c) follows from substituting $v+h_{\rm u}^2\to p$.

Using the fact that $Z\sim \mathrm{Exp}(1)$ and (V.2), the following integral can be evaluated as

$$\begin{aligned}\int_0^\infty\mathbb{P}\left\{Z\le sp^{-\frac{\alpha_{\rm u}}{2}}\right\}\mathrm{d}p &= \int_0^\infty\mathbb{P}\left[p<\left(\frac{s}{Z}\right)^{\frac{2}{\alpha_{\rm u}}}\right]\mathrm{d}p\\ &\overset{(a)}{=}\mathbb{E}\left[\left(\frac{s}{Z}\right)^{\frac{2}{\alpha_{\rm u}}}\right]\\ &= s^{\frac{2}{\alpha_{\rm u}}}\Gamma\left(1-\frac{2}{\alpha_{\rm u}}\right),\end{aligned} \tag{V.3}$$

where (a) follows from the identity, $\mathbb{E}[Z]=\int_0^\infty\mathbb{P}(Z>z)\mathrm{d}z$ for a non-negative random variable Z. Using (V.3) and (V.2), we complete the proof of the expression in (24).

Next, the Laplace transform of $\widetilde{T}_1$ is obtained as

$$\mathcal{L}_{\widetilde{T}_1}(s)=\mathcal{L}_{\widetilde{T}_0}(s)\mathbb{E}\left[\prod_{x\in\Psi'_{\rm g}(\mathcal{D})}e^{-sf(x)}\mid\Psi'_{\rm g}(\mathcal{D})\neq 0\right],$$

where $f(x)=\|(y_{\rm s},h_{\rm u})-(x,0)\|^{-\alpha_{\rm u}}$. Since the points of $\Psi'_{\rm g}(\mathcal{D})$ on $\mathcal{D}$ follow homogeneous PPP, using the PGFL for the conditioned Poisson random variable,

$$\begin{aligned}&\mathbb{E}\left[\prod_{x\in\Psi'_{\rm g}(\mathcal{D})}e^{-sf(x)}\mid\Psi'_{\rm g}(\mathcal{D})\neq 0\right]\\ &=\frac{\exp\left(-\lambda_{\rm g}\int_{\mathcal{D}}(1-e^{-sf(x)})\mathrm{d}x\right)-e^{-\lambda_{\rm g}|\mathcal{D}|}}{1-e^{-\lambda_{\rm g}|\mathcal{D}|}}\\ &\overset{(a)}{=}\frac{\exp\left(-\pi\lambda_{\rm g}\int_{h_{\rm u}^2}^{R_s^2}\left(1-e^{-sp^{-\frac{\alpha_{\rm u}}{2}}}\right)\mathrm{d}p\right)-e^{-\pi\lambda_{\rm g}(R_{\rm s}^2-h_{\rm u}^2)}}{1-e^{-\pi\lambda_{\rm g}(R_{\rm s}^2-h_{\rm u}^2)}},\end{aligned} \tag{V.4}$$

where $|\mathcal{D}|$ denotes the area of $\mathcal{D}$, (a) follows from the similar derivation in (V.2).

B. PROOF OF LEMMA 3

The Laplace transform of the total interference-plus-noise ratio at the typical UAV user is

$$\mathcal{L}_{\widetilde{\Upsilon}}(s)=\mathcal{L}_{\hat{I}_{\rm g}}(s)\mathcal{L}_{\hat{I}_{\rm u}}(s)e^{-s\sigma_{\rm n}^2}. \tag{V.5}$$

The Laplace transform of the aggregate interference from the GBS network received by the typical UAV user, where the GBSs follow a homogeneous PPP, is given by [31]

$$\mathcal{L}_{\hat{I}_{\rm g}}(s)=\exp\left(-\frac{\pi\lambda_{\rm g}(sP_{\rm g})^{\frac{2}{\alpha_{\rm g}}}}{\mathrm{sinc}\left(\frac{2}{\alpha_{\rm g}}\right)}\right). \tag{V.6}$$

Similarly, the Laplace transform of the aggregate interference from the GBS network received by the typical GBS user, conditioned on the distance between the user and its serving GBS x_o, is given by

$$\mathcal{L}_{I_{\rm g}|r_{\rm g}^2}(s)=\exp\left(-\pi\lambda_{\rm g}\int_{r_{\rm g}^2}^{\infty}\frac{sP_{\rm g}}{sP_{\rm g}+v^{\frac{\alpha_{\rm g}}{2}}}\mathrm{d}v\right), \tag{V.7}$$

where $r_{\rm g}^2$ denotes the squared distance between the user and the serving GBS. Using the derivation in (V.3), we obtain (51) as stated in Lemma 3.

The Laplace transform of $\hat{I}_{\rm u}$ is derived by following the procedure in Theorem 1. While Theorem 1 considers the mean channel power gain, the expression here incorporates the random channel gain defined in (3). This result is similar to that derived in (41), except for the change in the lower integration limit:

$$\begin{aligned}&\mathcal{L}_{\hat{I}_{\rm u}|r_{\rm u}^2}(s)\\ &=\exp\left(-\pi\gamma\lambda_{\rm u}\int_{r_{\rm u}^2+h_{\rm u}^2}^{\infty}\left\{\frac{sP_{\rm u}}{sP_{\rm u}+v^{\frac{\alpha_{\rm u}}{2}}}-\zeta\left(\sin^{-1}\frac{h_{\rm u}}{\sqrt{v}}\right)\right.\right.\\ &\quad\left.\left.\times\left[\left(1+\frac{sP_{\rm u}}{mv^{\frac{\alpha_{\rm u}}{2}}}\right)^{-m}-\frac{1}{1+sP_{\rm u}v^{-\frac{\alpha_{\rm u}}{2}}}\right]\right\}\mathrm{d}v\right),\end{aligned} \tag{V.8}$$

where $r_{\rm u}^2$ is the squared distance between the user and the ground projection of the serving UAV $(y_z,h_{\rm u})$.

Likewise, the Laplace transform of the aggregate interference from the UAV network to the typical GBS user is given by

$$\begin{aligned}&\mathcal{L}_{I_{\rm u}}(s)\\ &=\exp\left(-\pi\gamma\lambda_{\rm u}\int_{h_{\rm u}^2}^{\infty}\left\{\frac{sP_{\rm u}}{sP_{\rm u}+v^{\frac{\alpha_{\rm u}}{2}}}-\zeta\left(\sin^{-1}\frac{h_{\rm u}}{\sqrt{v}}\right)\right.\right.\end{aligned}$$

$$\times \left[\left(1+\frac{sP_{\rm u}}{mv^{\frac{\alpha_{\rm u}}{2}}}\right)^{-m} - \frac{1}{1+sP_{\rm u}v^{-\frac{\alpha_{\rm u}}{2}}}\right]\Bigg\}\mathrm{d}v\Bigg). \tag{V.9}$$

Substituting the expressions for the Laplace transforms completes the proof of Lemma 3.

REFERENCES

[1] G. K. Pandey, D. S. Gurjar, S. Yadav, Y. Jiang, and C. Yuen, "UAV-assisted communications with RF energy harvesting: A comprehensive survey," *IEEE Commun. Surveys Tuts.*, vol. 27, no. 2, pp. 782–838, 2025.

[2] N. Deng, H. Wei, and M. Haenggi, "Modeling and analysis of air-ground integrated networks with flexible beam coverage," *IEEE Trans. Wireless Commun.*, vol. 22, no. 11, pp. 8170–8184, 2023.

[3] N. Deng, R. Wu, M. Haenggi, H. Wei, and N. Zhao, "Air-ground cooperation for cell-corner users," *IEEE Trans. Wireless Commun.*, vol. 24, no. 7, pp. 5946–5960, 2025.

[4] M. Matinmikko-Blue, S. Yrjölä, and P. Ahokangas, "Spectrum management for local mobile communication networks," *IEEE Commun. Mag.*, vol. 61, no. 7, pp. 60–66, 2023.

[5] P. Yang, L. Kong, and G. Chen, "Spectrum sharing for 5G/6G URLLC: Research frontiers and standards," *IEEE Commun. Standards Mag.*, vol. 5, no. 2, pp. 120–125, 2021.

[6] Z. Sun, W. Liang, F. Qi, Z. Dong, and Y. Cai, "Blockchain-based dynamic spectrum sharing for 6G UIoT networks," *IEEE Netw.*, vol. 35, no. 5, pp. 143–149, 2021.

[7] A. Rabbachin, T. Q. Quek, H. Shin, and M. Z. Win, "Cognitive network interference," *IEEE J. Sel. Areas Commun.*, vol. 29, no. 2, pp. 480–493, 2011.

[8] Integrated sensing and communication unlocks spatial location of objects. [Online]. Available: https://www.ericsson.com/en/blog/2024/6/integrated-sensing-and-communication-unlocks

[9] C.-H. Lee and M. Haenggi, "Interference and outage in Poisson cognitive networks," *IEEE Trans. Wireless Commun.*, vol. 11, no. 4, pp. 1392–1401, 2012.

[10] B. Shang, L. Liu, H. Chen, C. J. Zhang, S. Pudlewski, E. S. Bentley, and J. D. Ashdown, "Spatial spectrum sensing in uplink two-tier user-centric deployed hetnets," *IEEE Trans. Wireless Commun.*, vol. 19, no. 12, pp. 7957–7972, 2020.

[11] H. Chen, L. Liu, T. Novlan, J. D. Matyjas, B. L. Ng, and J. Zhang, "Spatial spectrum sensing-based device-to-device cellular networks," *IEEE Trans. Wireless Commun.*, vol. 15, no. 11, pp. 7299–7313, 2016.

[12] H. Chen, L. Liu, H. S. Dhillon, and Y. Yi, "QoS-aware D2D cellular networks with spatial spectrum sensing: A stochastic geometry view," *IEEE Trans. Commun.*, vol. 67, no. 5, pp. 3651–3664, 2019.

[13] H. ElSawy and E. Hossain, "Two-tier hetnets with cognitive femtocells: Downlink performance modeling and analysis in a multichannel environment," *IEEE Trans. Mobile Comput.*, vol. 13, no. 3, pp. 649–663, 2014.

[14] Z. Yazdanshenasan, H. S. Dhillon, M. Afshang, and P. H. J. Chong, "Poisson hole process: Theory and applications to wireless networks," *IEEE Trans. Wireless Commun.*, vol. 15, no. 11, pp. 7531–7546, 2016.

[15] B. Shang, X. Huang, X. Li, C. Yang, X. Chu, and H. Zhang, "Spectrum sharing for satellite-terrestrial integrated networks: A spherical Poisson hole process-based approach," *IEEE Open J. Commun. Soc.*, vol. 7, pp. 2013–2033, 2026.

[16] Z. Wei, L. Wang, Z. Gao, H. Wu, N. Zhang, K. Han, and Z. Feng, "Spectrum sharing between high altitude platform network and terrestrial network: Modeling and performance analysis," *IEEE Trans. Commun.*, vol. 71, no. 6, pp. 3736–3751, 2023.

[17] D. Kim, J. Park, J. Choi, and N. Lee, "Spectrum sharing between low earth orbit satellite and terrestrial networks: A stochastic geometry perspective analysis," *IEEE Trans. Wireless Commun.*, vol. 25, pp. 8905–8921, 2026.

[18] N. Okati, A. Noll Barreto, L. Uzeda Garcia, and J. Wigard, "Co-existence analysis of terrestrial and non-terrestrial networks in S-band using stochastic geometry," *IEEE Trans. Commun.*, vol. 74, pp. 4431–4445, 2026.

[19] S. R. Sabuj, D. K. P. Asiedu, K.-J. Lee, and H.-S. Jo, "Delay optimization in mobile edge computing: Cognitive UAV-assisted eMBB and mMTC services," *IEEE Trans. on Cogn. Commun. Netw.*, vol. 8, no. 2, pp. 1019–1033, 2022.

[20] Z. Wei, J. Zhu, Z. Guo, and F. Ning, "The performance analysis of spectrum sharing between UAV enabled wireless mesh networks and ground networks," *IEEE Sensors J.*, vol. 21, no. 5, pp. 7034–7045, 2021.

[21] M. M. Azari, G. Geraci, A. Garcia-Rodriguez, and S. Pollin, "UAV-to-UAV communications in cellular networks," *IEEE Trans. Wireless Commun.*, vol. 19, no. 9, pp. 6130–6144, 2020.

[22] C. Zhang and W. Zhang, "Spectrum sharing for drone networks," *IEEE J. Sel. Areas Commun.*, vol. 35, no. 1, pp. 136–144, 2017.

[23] F. Shen, G. Ding, Z. Wang, and Q. Wu, "UAV-based 3D spectrum sensing in spectrum-heterogeneous networks," *IEEE Trans. Veh. Technol.*, vol. 68, no. 6, pp. 5711–5722, 2019.

[24] B. Shang, L. Liu, R. M. Rao, V. Marojevic, and J. H. Reed, "3D spectrum sharing for hybrid D2D and UAV networks," *IEEE Trans. Commun.*, vol. 68, no. 9, pp. 5375–5389, 2020.

[25] M. A. Syed, H. Li, E. J. Knoblock, and L. Liu, "Spectrum sensing in UAV-enabled cellular networks," in *2025 IEEE International Conference on Communications Workshops (ICC Workshops)*, 2025, pp. 971–976.

[26] S. N. Chiu, D. Stoyan, W. S. Kendall, and J. Mecke, *Stochastic Geometry and Its Applications*, 3rd ed. New York: John Wiley and Sons, Inc., 2013.

[27] A. Al-Hourani, S. Kandeepan, and S. Lardner, "Optimal LAP altitude for maximum coverage," *IEEE Wireless Commun. Lett.*, vol. 3, no. 6, pp. 569–572, Dec. 2014.

[28] M. K. Steven, *Fundamentals of Statistical Signal Processing, Volume II: Detection Theory*. Englewood Cliffs, NJ: PTR Prentice-Hall, 1998.

[29] J. Abate and W. Whitt, "A unified framework for numerically inverting Laplace transforms," *INFORMS Journal on Computing*, vol. 18, no. 4, pp. 408–421, 2006.

[30] Z. Chen, C.-X. Wang, X. Hong, J. S. Thompson, S. A. Vorobyov, X. Ge, H. Xiao, and F. Zhao, "Aggregate interference modeling in cognitive radio networks with power and contention control," *IEEE Trans. Commun.*, vol. 60, no. 2, pp. 456–468, 2012.

[31] M. Haenggi, *Stochastic geometry for wireless networks*. Cambridge University Press, 2012.

[32] C.-H. Liu, K.-H. Ho, and J.-Y. Wu, "mmWave UAV networks with multi-cell association: Performance limit and optimization," *IEEE J. Sel. Areas Commun.*, vol. 37, no. 12, pp. 2814–2831, 2019.

[33] E. L. Lehmann, "Some concepts of dependence," in *Selected Works of EL Lehmann*. Springer, 2011, pp. 815–831.

[34] K. A. Hamdi, "A useful lemma for capacity analysis of fading interference channels," *IEEE Trans. Commun.*, vol. 58, no. 2, pp. 411–416, 2010.

MD ASIF SYED (Senior Member, IEEE) received the B.Sc. degree in electronics and communication engineering from Khulna University, Bangladesh, the M.E. degree in information and communication engineering from Inha University, South Korea, and the M.Sc. degree in electrical and computer engineering from Mississippi State University, USA. He is currently pursuing the Ph.D. degree in electrical and computer engineering at the University of Louisville, USA. His research interests include wireless communications, information theory, machine learning, and signal processing.

HONGXIANG LI (Senior Member, IEEE) received his Ph.D. in Electrical Engineering from the University of Washington, Seattle, in 2008. He is currently a Professor in the Department of Electrical and Computer Engineering at the University of Louisville. In recent years, his work has focused on the application of machine learning to communication systems and spectrum optimization. His research has been funded by the NSF, NASA, and ONR, and he has authored over 150 peer-reviewed journal and conference papers. Dr. Li received the ORAU Ralph E. Powe Junior Faculty Enhancement Award in 2012. He served as a Visiting Faculty Member at the Air Force Research Laboratory in Rome, NY, in 2012 and 2018. Dr. Li was also a NASA Glenn Faculty Fellowship Program (NGFFP) Awardee in 2013, 2018, 2019, and 2025, contributing to research on transceiver design, delay-sensitive aerial V2V communications, and aeronautical spectrum optimization. He previously served as an Editor for IEEE Communications Letters.

MARTIN HAENGGI (Fellow, IEEE) received the Dipl.-Ing. (M.Sc.) and Dr.sc.techn. (Ph.D.) degrees in electrical engineering from the Swiss Federal Institute of Technology in Zurich (ETHZ) in 1995 and 1999, respectively. Currently he is the Freimann Professor of Electrical Engineering and a Concurrent Professor of Applied and Computational Mathematics and Statistics at the University of Notre Dame, Indiana, USA. In 2007-2008, he was a Visiting Professor at the University of California at San Diego, in 2014-2015 he was an Invited Professor at EPFL, Switzerland, and in 2021-2022 he was a Guest Professor at ETHZ. He is a co-author of the monographs "*Interference in Large Wireless Networks*" (NOW Publishers, 2009) and "Stochastic Geometry Analysis of Cellular Networks" (Cambridge University Press, 2018) and the author of the textbook "*Stochastic Geometry for Wireless Networks*" (Cambridge, 2012) and the blog stogblog.net. His scientific interests lie in networking and wireless communications, with an emphasis on cellular, amorphous, ad hoc (including D2D and M2M), cognitive, vehicular, and wirelessly powered networks. He served as an Associate Editor for the Elsevier Journal of Ad Hoc Networks, the IEEE Transactions on Mobile Computing (TMC), the ACM Transactions on Sensor Networks, as a Guest Editor for the IEEE Journal on Selected Areas in Communications, the IEEE Transactions on Vehicular Technology, and the EURASIP Journal on Wireless Communications and Networking, as a Steering Committee member of the TMC, and as the Chair of the Executive Editorial Committee of the IEEE Transactions on Wireless Communications (TWC). From 2017 to 2018, he was the Editor-in-Chief of the TWC. For both his M.Sc. and Ph.D. theses, he was awarded the ETH medal. He also received a CAREER award from the U.S. National Science Foundation in 2005 and three paper awards from the IEEE Communications Society, the 2010 Best Tutorial Paper award, the 2017 Stephen O. Rice Prize paper award, and the 2017 Best Survey paper award, and he is a Clarivate Analytics Highly Cited Researcher.

ERIC J. KNOBLOCK received the B.S. and M.S. degrees in electrical engineering from Cleveland State University, Cleveland, OH, USA, in 1999 and 2000, respectively, and the Ph.D. degree in electrical engineering from the University of Akron, Akron, OH, USA, in 2026. He is a Branch Manager in the Communications and Intelligent Systems Division at the NASA Glenn Research Center, Cleveland, OH, USA. His research interests include the application of machine learning and artificial intelligence to aerospace communication systems. He is a registered Professional Engineer in the state of Ohio.

